**The Thesis Committee for Justin Andrew Spurbeck**
**Certifies that this is the approved version of the following Thesis:**

# Near Real Time Satellite Event Detection, Characterization, and Operational Assessment via the Exploitation of Remote Photoacoustic Signatures

**APPROVED BY**
**SUPERVISING COMMITTEE:**

Moriba K. Jah, Supervisor

Brandon A. Jones

# Near Real Time Satellite Event Detection, Characterization, and Operational Assessment via the Exploitation of Remote Photoacoustic Signatures

**by**

**Justin Andrew Spurbeck**

**Thesis**

Presented to the Faculty of the Graduate School of

The University of Texas at Austin

in Partial Fulfillment

of the Requirements

for the Degree of

**Master of Science in Engineering**

**The University of Texas at Austin**

**May 2019**

*To my parents, grandparents, Aunt Wendy, and Uncle Mark.*

*"Newton's Third Law…you gotta leave something behind."*

*- Joseph A. Cooper*

## Acknowledgements

I would like to thank my advisor Dr. Moriba Jah for giving me the opportunity to continue my education in graduate school and for stimulating many collaborative connections made along the way, for without them this thesis would not have been possible. Additionally, I would like to give my sincerest thank you to our colleagues at SERC and EOS Space Systems, specifically Dr. James Bennett, Dr. James Webb, and Dr. Daniel Kucharski, for the data collection and hypertemporal sampling detector operations. None of the experimental observations would have been possible without this collaboration, kangaroos included. I would also like to note that I have adopted the term "rip-snorter" as a direct consequence of the Australian influence throughout this work.

Another sincere thank you is deserved of Andrew Edwards, Tim Lilley, Anthony Belo, and the rest of the team at Optus for providing the necessary collaboration and data to support this research. And to the operators at Iridium, specifically Ryan Shepperd and Misa Iovanov among others, thank you for the willing collaboration and data analysis. I would also like to thank Dr. Tamara Payne for valuable discussions regarding synthetic light curve simulations and atmospheric noise assumptions as well as Dr. Preston Wilson for pointing me towards the cross-correlation methodology and for fruitful discussions on acoustics.

And to Dr. Brandon Jones, thank you for taking the time to be on my supervising committee and for showing interest in my research. Also, a sincere thank you is required of my DigitalGlobe colleagues for allowing me to split time between work, graduate school, and research. I would also like to thank Mike Nicolls of LeoLabs for the brief maneuver detection support and helpful supplementary data analysis.

Finally, I would like to thank my parents for all the support and encouragement along the winding road that is graduate school. The many phone calls, care packages, and trips to visit home were welcome milestones to look forward to during this journey. This thesis would not have been possible without you. I would also like to sincerely thank my grandparents again for their continual support throughout my academic career.

To all the other family, friends, roommates, professors, colleagues, classmates, and my siblings – thank you for making this journey much more enjoyable. To my Aunt Wendy, thank you for giving me the initial inspiration to pursue aerospace engineering as a career path and for the second home while living in Colorado. And to my Uncle Mark, thanks for teaching me how to go big.

# Abstract

## Near Real Time Satellite Event Detection, Characterization, and Operational Assessment via the Exploitation of Remote Photoacoustic Signatures

Justin Andrew Spurbeck, M.S.E.

The University of Texas at Austin, 2019

Supervisor: Moriba K. Jah

Active satellites frequently maneuver to maintain nominal mission orbits and to mitigate conjunctions with debris or other active spacecraft. With an ever-growing Resident Space Object (RSO) population, the need to detect and predict changes in active satellite trajectories has become increasingly important. Satellite behavior typically produces a lag on the order of hours to days from time of maneuver to unmodeled dynamic event detection depending on the magnitude of the $\Delta v$. For uncooperative objects, this detection lag poses a hazard to other satellites. Implementing an active photoacoustic signature change detection methodology to detect and predict unmodeled dynamic events can reduce the overall conjunction risk and provide a means for a near real time pulse of satellite events.

Remote photoacoustic sensing is defined herein as the acoustic playback of hypertemporal photometric data. This thesis demonstrates the conversion of both photometric and luminance data into the acoustic domain in support of RSO

characterization. If photometric data is collected at a kilohertz (kHz) level sampling rate, optimally above 40 kHz, any changes in outgoing photon flux due to satellite body vibrations caused by on-board events may be detected. Using the detected event epochs allows for accurate estimation of the $\Delta v$, direction, and maneuver type in near real time. The analysis of hypertemporal light curve data in the photometric, frequency, and photoacoustic domains can thus help characterize the event and provide mission-specific intelligence.

This thesis also investigates the use of signal processing methods, primarily cross-correlation, to improve the minimum vibration-induced satellite body displacement detection threshold in the presence of noise generated by the turbulent atmosphere. In addition to the basic parameters related to the $\Delta v$ calculation, it is shown that thruster mass flow rate, fuel consumption, exhaust velocity, and specific impulse can be derived with a sufficiently accurate and precise *a priori* estimate of mass. The operational assessment and satellite characterization made possible by remote photoacoustic sensing ultimately provides a means to support a more sustainable space environment for long-term human space flight operations.

# Table of Contents

# List of Tables

# List of Figures

# Nomenclature

Any variable not listed in this section is either defined in its chapter or assumed known by context or first principles. Unit vectors are denoted with a hat superscript and standard vectors with a bar, leaving the corresponding scalars without a bar accent.

| | | | |
|---|---|---|---|
| $A_i$ | Satellite face surface area | $h_f$ | Final momentum wheel value |
| $A_{sp}$ | Solar panel surface area | $\bar{h}$ | Specific orbital momentum |
| $\bar{a}_{th}(t)$ | Thrust vector as function of time | $H_k$ | Measurement partials matrix |
| $\hat{a}_{th}(t)$ | Unit thrust vector as func. of time | $I_i$ | Initial mass moment of inertia |
| $c$ | Speed of light | $I_f$ | Final mass moment of inertia |
| $C_{d,i}$ | Diffuse reflectance coefficient | $I_{sp}$ | Specific impulse |
| $C_D$ | Drag coefficient | $K_k$ | Kalman gain matrix |
| $C_{l,m}$ | Spherical harmonics gravity coef. | $L$ | Sun to RSO angle |
| $C_{s,i}$ | Specular reflectance coefficient | $\bar{L}(t)$ | Angular work |
| $d_{box}$ | Peak box-shear displacement | $\lambda_{sat}$ | Satellite longitude |
| $d_{sp}$ | Peak solar panel displacement | $m$ | Mass of spacecraft |
| $\Delta m$ | Fuel consumed by maneuver | $m_i$ | Initial satellite mass |
| $\Delta t$ | Impulse duration | $m_f$ | Final satellite mass |
| $\Delta v$ | Change in velocity | $m_{v,sun}$ | Apparent visual mag. of Sun |
| $\varepsilon_i$ | Initial specific energy | $m_{v,object}$ | Apparent visual mag. of RSO |
| $\varepsilon_f$ | Final specific energy | $\dot{m}$ | Mass flow rate |
| $\Gamma$ | Process noise transition matrix | $\mu$ | Earth's gravitational constant |
| $g_0$ | Standard gravity | $\mu_M$ | Moon's gravitational constant |
| $h_i$ | Initial momentum wheel value | $\mu_S$ | Sun's gravitational constant |

| | | | |
|---|---|---|---|
| $N_i$ | Normal facet unit vector | $\rho_d$ | Range from observer to satellite |
| $N_{v,atm}$ | Gaussian dist. of atm. noise | $\rho_b$ | Range bias |
| $N(t)$ | Nutation rotation matrix | $r$ | Magnitude of position vector |
| $\omega$ | Event frequency | $\bar{r}_i$ | Initial position at maneuver start |
| $\omega_E$ | Rotation rate of the Earth | $\bar{r}_f$ | Final position at maneuver end |
| $\bar{\omega}_i$ | Initial satellite angular velocity | $\bar{r}(t)$ | Position throughout maneuver |
| $\bar{\omega}_f$ | Final satellite angular velocity | $R_k$ | Measurement noise |
| $P(t)$ | Precession rotation matrix | $R_n(\phi)$ | Rot. matrix for surf. unit vector |
| $P_{l,m}$ | Legendre functions | $R(t)$ | Sidereal time rotation matrix |
| $p_{srp}$ | Solar pressure coefficient | $R_E$ | Radius of Earth |
| $P_k$ | State covariance matrix | $S_i$ | Intensity of light refl. in obs. dir. |
| $P_{zz}$ | Innovations covariance matrix | $S_{l,m}$ | Spherical harmonics gravity coeff. |
| $\bar{P}_k$ | Linear propagation of covariance | $\sigma_{v,atm}$ | Standard deviation of atm. noise |
| $\phi$ | Rotation/shear angle of box-wing | $\sigma_{v,sig}$ | Standard dev. of event signal |
| $\phi_{fpa}$ | Flight path angle | $\theta_i$ | Incidence angle |
| $\phi_{gc,sat}$ | Geocentric latitude | $t$ | Time (since epoch) |
| $\phi_{max}$ | Max shear/rotation angle | $t_{burn}$ | Epoch of maneuver rel. to initial |
| $\phi_{v,sp}$ | Solar panel to velocity angle | $t_i$ | Initial maneuver event epoch |
| $\phi(t_f,t_i)$ | State transition matrix | $t_f$ | Final maneuver event epoch |
| $Q_{k-1}$ | Process noise covariance matrix | $t_{l,a}$ | Apparent light time |
| $Q$ | Cross-correlation magnitude | $t_{l,c}$ | Corrected light time |
| $\rho$ | Atmospheric density | $\bar{\tau}(t)$ | Torque vector as function of time |
| $\rho_a$ | Apparent range | $U_E$ | Gravitational potential energy |
| $\dot{\rho}_a$ | Apparent range rate | $\hat{\mathrm{u}}_{\mathrm{osc}}(\mathrm{t})$ | Inst. surface unit normal vector |

| | |
|---|---|
| $\hat{\mathrm{u}}_{\mathrm{srf}}(\mathrm{t})$ | Nominal surface unit normal vec. |
| $\bar{v}_i$ | Velocity at maneuver start epoch |
| $\bar{v}_f$ | Velocity at maneuver end epoch |
| $\bar{v}(t)$ | Velocity throughout impulse |
| $\bar{v}_{rel}$ | Velocity relative to moving atm. |
| $v_{rel}$ | Magnitude of rel. velocity vector |
| $V$ | RSO to observer unit vector |
| $W(t)$ | Polar motion rotation matrix |
| $\hat{x}_k$ | Measurement updated state |
| $\bar{x}_k$ | Propagated state |
| $z_k$ | Measurements |

# Chapter 1

# Introduction

The space environment near Earth has grown crowded since the dawn of the space age in the late 1950s. Technological advances and decreases in manufacturing costs have led to a significant increase in the space object population visualized in Fig. 1. Increased launch frequency by government agencies and the private sector coupled with the sheer number of uniquely controlled payloads that can be included per launch demonstrate the need for a robust system to monitor and protect the space environment. Companies like OneWeb and SpaceX plan to launch thousands of satellites to fill their kilo constellations in the next decade, raising questions on autonomous conjunction assessment capabilities. The Chinese anti-satellite (ASAT) missile test in 2007, the Iridium-Cosmos collision in 2009, and the Indian ASAT test in 2019 each created thousands of pieces of debris and forced space operators to reevaluate their preparedness for such events.

A challenge inherit to the crowded orbital environment is how to effectively predict collision risks and utilize that information to ensure active satellite survival and compliance with the Inter-Agency Space Debris Coordination Committee guidelines. Space debris mapping entities such as LeoLabs and the Combined Space Operations Center (CSpOC) provide conjunction data messages via a global array of sensors to operators with assets that have secondary Resident Space Objects (RSOs) within their screening volume. The operators will utilize this information to maneuver their assets into a safer orbit if required.

A responsible satellite operator will send a predicted ephemeris including a planned maneuver to CSpOC such that it can be preemptively screened against any other

secondary RSOs. The screening is to ensure the maneuver does not put the satellite into the path of another object, effectively defeating the purpose of the collision avoidance maneuver. There are, however, instances where an operator does not follow this procedure, and thus maneuvers and potential conjunctions are unpredictable.

When an active spacecraft performs a maneuver, it can take a tracking entity like CSpOC on the order of hours or sometimes days to detect an unmodeled dynamic event assumed to be a maneuver ($\Delta v$). This event detection lag demonstrates the opportunity for an improved method to quickly determine when an uncooperative RSO has maneuvered and estimate its new trajectory. If there were such a method, it would not only help reduce potential conjunction risks much sooner, it would also provide data that would allow satellite operational capability assessments useful for mission characterization and intelligence gathering.

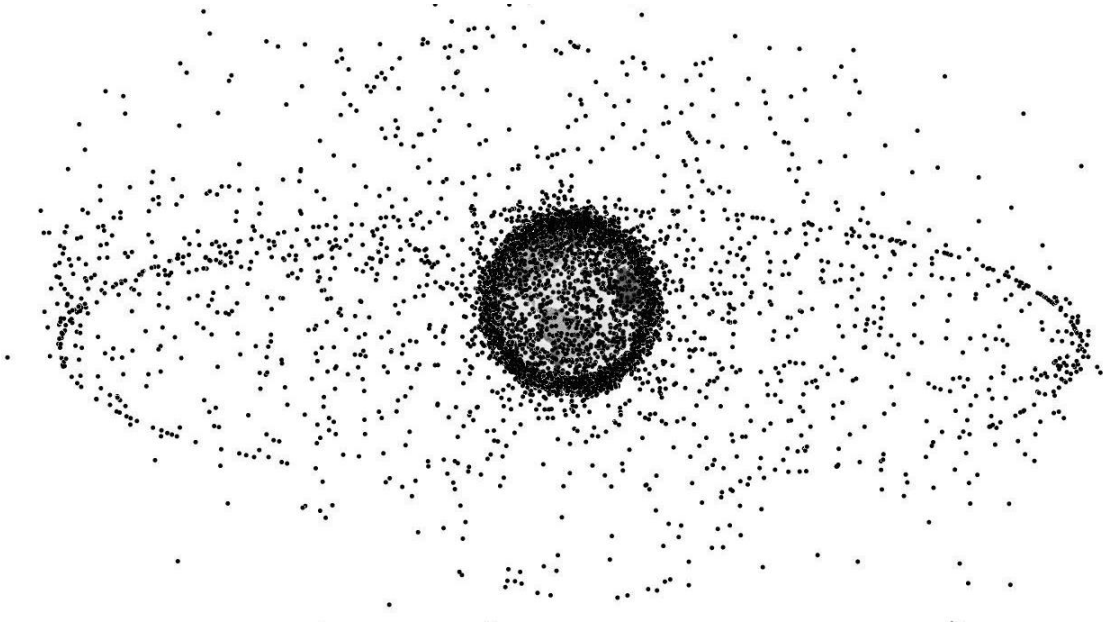

Figure 1: Visualization of the 18,500 uniquely tracked space object population. Image from the NASA Orbital Debris Program Office.

In addition to the detection lag, determination of what type of on-board event that occurs is difficult, if not impossible, with current remote sensing techniques. If the trajectory of an RSO is not sufficiently perturbed by a space event, it will likely go unnoticed. Aside from the need for near real time monitoring of active satellites, there are gaps in how both active and inactive RSOs are characterized and uniquely identified. Any source of data that would provide unique signature identifiers based on RSO shape, behavior, mass, or other parameters increases industry capability to better understand the RSO population. Ultimately, the goal of any scientific research in the orbital debris and Space Domain Awareness (SDA) communities is to maintain a sustainable space environment for long term human spaceflight operations. Potential runaway orbital debris scenarios such as the Kessler syndrome add a sense of urgency and responsibility shared with all space operators. Dependency of the human race on space-based systems such as the Global Positioning System (GPS), reliance on actionable geospatial data for disaster response, and daily use of detailed maps of Earth's surface confirm the importance of continued research and funding for SDA efforts.

The research presented herein seeks to further knowledge in the aforementioned problem areas and is structured as follows. Chapter 2 defines photoacoustic signatures and the fundamentals of acoustic data. This section also demonstrates a conversion technique using multiple data sources as a proof of concept. Chapter 3 performs a literature review of current state of the art techniques and postulates applications of photoacoustic sensing to support space event identification and RSO characterization. Chapter 4 demonstrates how hypertemporal photometric data can be used to detect minute vibrations on-board active spacecraft. The method is then extended to combat unfavorable turbulent atmospheric effects by implementing advanced signal processing

techniques. Chapter 5 utilizes the knowledge gained in Chapter 4 to estimate $\Delta v$ and maneuver-related parameters in near real time. Chapter 6 continues the prior chapter's work by applying the principles of conservation of orbital energy and momentum to estimate thruster specific parameters such as mass flow rate and specific impulse. Chapter 7 presents the results and discussion relating to the experimental data collection efforts put forth by the Optus, Space Environment Research Centre (SERC), and EOS Space Systems teams. Chapter 8 summarizes the results of all research contained in this thesis and outlines opportunities for future photoacoustic sensing research.

# Chapter 2

## Remote Photoacoustic Signatures

The human ear is capable of discerning frequencies in the audible range of 20 Hz to 20 kHz. A vibrating object, like the diaphragm in a loudspeaker, generates pressure waves that propagate through a transmission medium such as air or water. The brain perceives these audible waves of pressure as sound because the waves vibrate small hair cells deep in the inner ear. These cells produce electrical impulses that are then sent to the brain via the auditory nerve. It was first shown by Alexander Graham Bell, inventor of the telephone, that a transmission medium is not necessary to reproduce audible pressure waves at a distance [1].

This phenomenon is quite useful in the collection of remote photometric data from objects in Earth orbit because there exists no medium for it to propagate through in the vacuum of space. An acoustic signal can be generated from the photometric data by converting the frequency content in the light curve to audio. To abide by the Nyquist Theorem, sampling at 40 kHz plus a safety margin would accurately recover all naturally discernable sound and avoid aliasing. Most compact discs, mp3 format audio, or other standard audio codecs are sampled at 44-48 kHz for the above reasons. Thus, the acoustic playback of hypertemporal photometric data is defined as its photoacoustic signature. The light to sound conversion is possible because the reflected photons carry an equivalent vibrational information content that an acoustic wave cannot, again because there is no medium for it to propagate through in the vacuum of space [2].

To generate a playable photoacoustic signature, an image sensor such as a charged-coupling device or fast photodiode samples reflected photon flux and digitizes light intensity values collected via optical telescope observations of a target RSO. These

single-channel light intensity values can then be converted to any one of the many standard audio codecs. The WAVE (.wav) format is chosen for this research due to its lossless quality, easy editing, and high dynamic range. Normalizing the light intensity time series between the values of 0 and 1 sufficiently adheres to the WAVE codec. Other normalization methods such as an 8 bit per sample data range of 0 to 255 would also be adequate. This conversion process allows for functions such as MATLAB's *audiowrite* to produce the desired .wav file output ready for acoustic playback. A computer then interprets the digitized values inside the .wav file and sends electric signals to a speaker that modulates its diaphragm proportionally to produce the pressure waves humans perceive as sound.

## GSSAP-ANGELS LAUNCH FOOTAGE

To test the light to sound conversion technique of an on-orbit satellite, an initial candidate dataset was identified in the form of an amateur video taken of the Milky Way. What appeared to be a final boost stage maneuver of the Geosynchronous Space Situational Awareness Program (GSSAP) and Automated Navigation and Guidance Experiment for Local Space (ANGELS) satellite launch was inadvertently detected by an astrophotographer generating a time lapse of the night sky in July 2014[1]. The final boost stage maneuver was of a large magnitude, long duration, and at a low enough altitude to detect with a digital camera. The result of tracking, isolating, and enhancing the video to analyze the luminance time series of the thruster event is shown in Fig. 2.

To convert the red-green-blue color triplets produced by the digital camera to luminance values, a standard derivation per the International Telecommunications Union

[1] Image data from Dakotalapse, *"Final Boost Stage of GSSAP and ANGELS satellites – 4K UHD,"* 6 Jan 2015. Accessed via https://www.youtube.com/watch?v=I0Eu5Jk9NGQ.

is employed [3]. The acoustic representation of the data is not representative of an authentic thruster fire event due to the video's low frame rate of 24.0 frames per second. The time lapse itself operated at one frame every three seconds, providing an effective acoustic source at only 8 Hz which is lower than any human's perceivable hearing range. The shift and scale methods used by the Mars InSight lander team discussed in later chapters were useless due to the limited time duration of the data. In some video production and visual effects suites, an interpolation method can be used to estimate pixel motion within a frame. The motion estimation can then be used to generate an intermediate frame or average of the two neighboring frames. While this method works well for non-flickering objects, applying interpolation to this footage would effectively be generating noise in between each frame as the true frequency content of the thruster event would remain unknown.

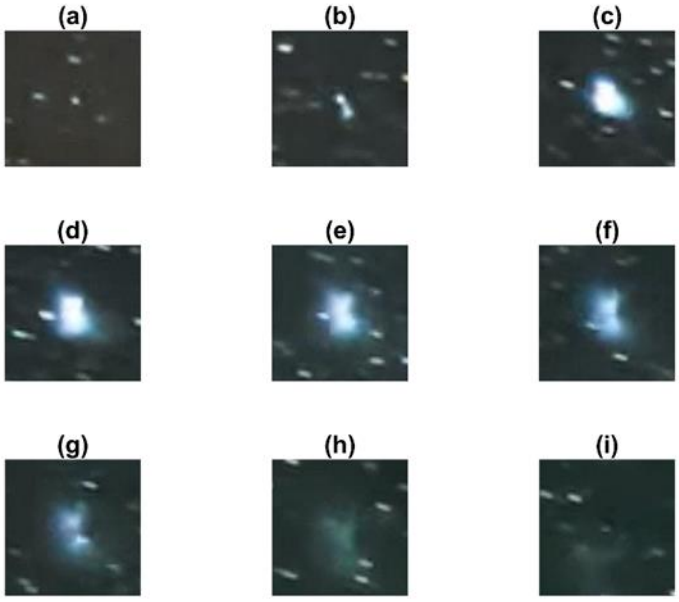


Figure 2: Cropped and stabilized frames of GSSAP-ANGELS footage showing *(a)* pre-event nominal behavior, *(b)* thruster ignition, *(c)-(f)* nominal thrust, and *(g)-(i)* plume dissipation.

## BLOODHOUND SSC ROCKET GROUND TEST

To prove that the video to sound conversion is a realistic process, the method is implemented on high frame rate ground test footage of a Bloodhound Supersonic (SSC) rocket[2]. The 4,000 frames per second rate is more suitable for a proof of concept as compared to the 8 Hz GSSAP-ANGELS source even though it contains only one second of real time playback. As before, a luminance time series is generated from various regions of the source frames in Fig. 3 as shown in Fig. 4. The time series of this data produces a realistic acoustic representation of the true rocket exhaust sound and stands as proof of concept for the light to sound conversion of an Earth-orbiting satellite firing its thrusters. It should be noted that although the acoustic representation's aesthetic is what is expected of a rocket fire event, the source data is effectively 2 kHz and thus only represents the lower end of audible frequencies. A real recording of similar tests would have the full range of human frequencies up to 20 kHz. Including the missing high frequency content would produce the most accurate reproduction of the acoustic source. The true sound of a Bloodhound SSC can be heard as in other publicly available data for comparison[3].

[2] Image data retrieved from iX Cameras, *"Bloodhound SSC rocket test 2,000 fps and 4,000 fps mono and color,"* 15 Feb 2017. Accessed via https://www.youtube.com/watch?v=61E0dprLMwk.

[3] Bloodhound SSC example footage retrieved from BLOODHOUND SSC – 1,000 mph car, *"BLOODHOUND's new 1,000mph Hybrid Rocket – Tested,"* 12 Dec 2014. Accessed via https://www.youtube.com/watch?v=Tk67Z_mai_k.

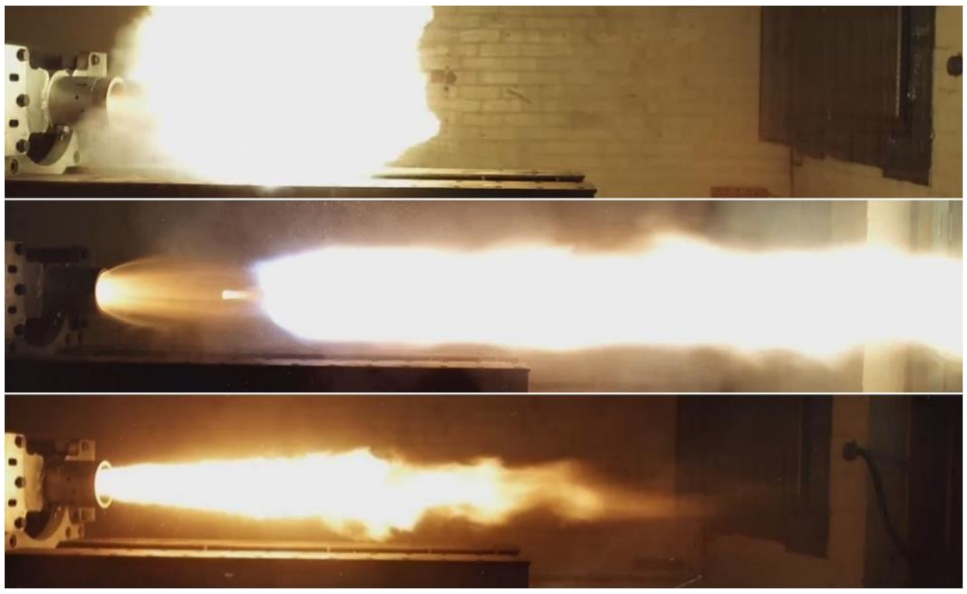

Figure 3: Bloodhound SSC Rocket ground test from[2] showing *(top)* ignition, *(middle)* near nominal thrust, and *(bottom)* plume dissipation.

Selection of which pixels to utilize to represent the frequency content of the plume should be conducted with caution. Depending on the video processing algorithm's formulation, selecting all available pixels can result in a frequency averaging effect which seems to decrease the realness of the audio. The tail of the Bloodhound SSC plume is the most turbulent section and thus most of the tested luminance time series were generated from vertical slices of the plume's tail. Larger pixel sections produced useable results as well. Due to camera proximity, the quality and uniqueness of the pixels used in the Bloodhound SSC footage were more suitable for audio generation compared to the highly cropped pixels in the GSSAP-ANGELS data.

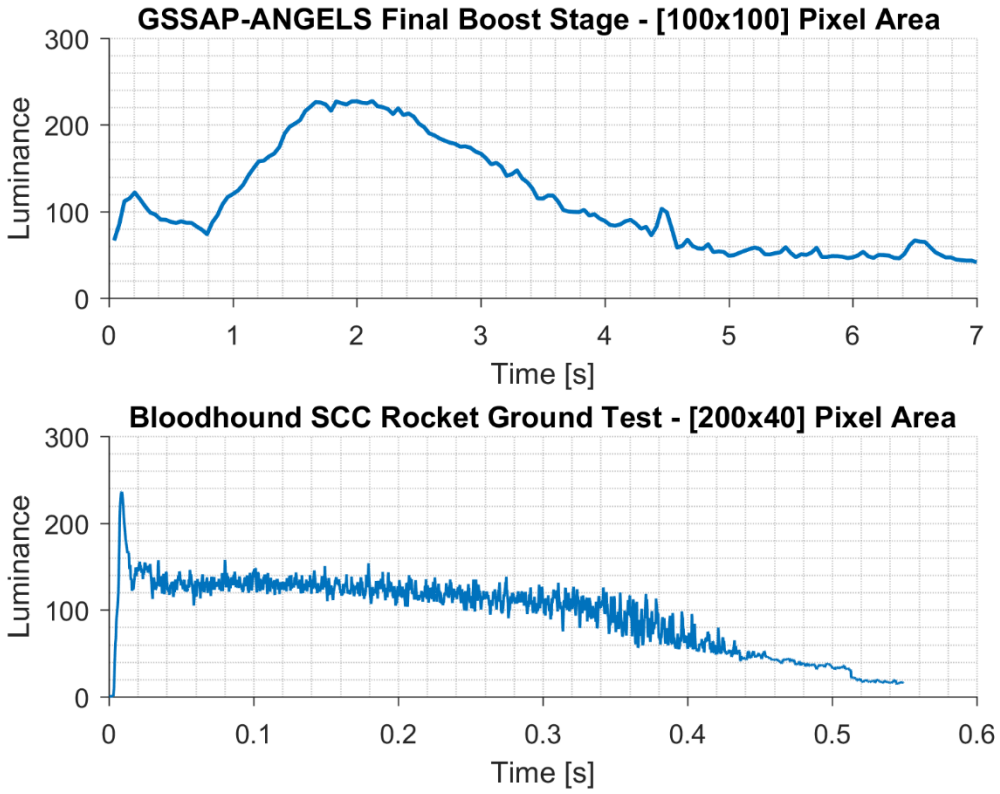


Figure 4: Luminance time series generated from source frames in Fig. 2 and Fig. 3.

## EXOANALYTICS IMAGERY

An example of the resolution that is currently possible for a geosynchronous observation of a satellite performing a maneuver is shown in Fig. 5, made publicly available by ExoAnalytics Solutions[4]. The image sequence shows various shockwave-like expulsions of propellant as well as a payload deployment, maneuver, and fuel dump. With a relative field of view (FOV) wide enough to distinguish these events visually, photoacoustic representation would not be necessary to determine this is a thruster event. However, for the subtler events like a small collision avoidance burn or for maneuvers

[4] Image data retrieved from ExoAnalytic Solutions Videos, *"Commercial Space Situational Awareness Solutions,"* 14 March 2018. Accessed via https://www.youtube.com/watch?v=kKQLiqM42Xw.

utilizing different classes of propulsion such as ion, pulsed, or plasma thrusters, the information will likely all be contained in a much smaller portion of the focal plane, essentially a few pixels, with no or barely visible plumes. This situation would require photometric frequency and photoacoustic signature analysis to characterize the physical event.

Like the GSSAP-ANGELS footage, the available data rate of approximately 8 Hz and duration of 16 seconds were below the threshold required to produce a realistic photoacoustic signature. If an event similar to the one captured in the ExoAnalytics imagery were sampled in the kilohertz range with the resolution displayed in Fig 5., it is plausible a realistic acoustic representation could be generated following the techniques presenting herein.

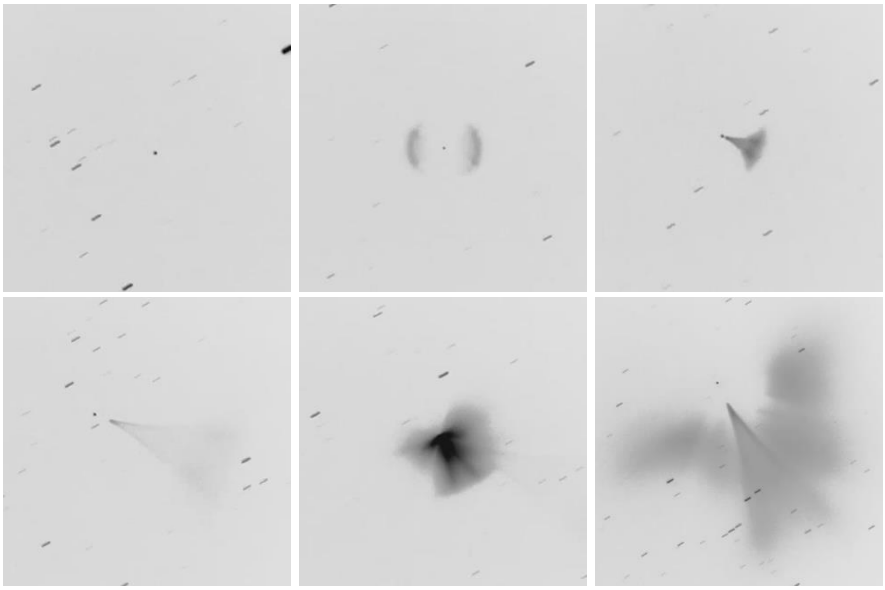

Figure 5: Image sequence publicly available from ExoAnalytics showing active satellite events in GEO. *(Top middle, right, bottom left)* payload jettison, deployment, *(bottom middle, right)* fuel dump and thruster plume visible.

# Chapter 3

# Resident Space Object Event Characterization

The use of sound may seem like a museum piece side effect of the photometric data frequency content analysis, but the perception of the data in the acoustic domain does yield important revelations. It turns out the human brain is an amazing pattern recognition machine that still outperforms computers in some signal identification applications [4]. Many audio processing systems are attempting to model how the brain's mechanisms can efficiently identify and understand certain signals that exist in the presence of complex background noise [5]. The benefit of sound analysis comes from correlation of an acoustic signature to a physical event, as demonstrated in the following literature review.

## PHOTOACOUSTIC SIGNATURE CASE STUDIES

One audio recovery technique proven robust in terrestrial based tests demonstrated the capability to accurately recover a conversation or song on the radio through sound proof glass. This was achieved by collecting and analyzing the light being modulated by a flexible surface nearby the acoustic source such as a plant leaf [6]. The direct analogy to applying photoacoustic sensing remotely is to imagine a satellite's solar panel as the leaf in this example and a thruster fire event as the acoustic source from the radio.

Another example as to how the acoustic interpretation of an inherently non-acoustic signal supported the characterization of a physical event is seen in the analysis of plasma wave data from the Voyager 1 spacecraft. The NASA mission scientists converted the vibrations of dense ionized gas detected by the plasma wave instrument

into sound. Conversion of this data to an acoustic signal helped gain insight into plasma transits that were previously thought to be unrelated events. When listening to the audio playback, the mission scientists noticed a unique rising tone in three separate spectrogram events. Noticing a correlation between these events helped infer a continuously increasing density profile, a detection of interstellar plasma, transit of the heliopause, and thus a departure from our Solar System [7].

A more recent demonstration of this technique was reported from NASA's Mars InSight lander a few days after it touched down on the Martian surface. The spacecraft's seismometer and air pressure instruments detected vibrations caused by a 10-15 mph wind blowing across Mars' Elysium Planitia [8]. Acoustic playback yielded a "haunting low rumble" which was shifted up two octaves and sped up by a factor of one hundred to produce discernable audible samples. The acoustic representation helped support claims consistent with a dust devil observed from Martian orbit near the landing area.

Yet another case of photoacoustic conversion is reported by Slater et al. in [9] showing that sound can be recovered across terrestrial distances of at least 80 km. Police sirens, public address systems, and brush fires were detected remotely using nearby natural acousto-optic modulators such as a car window. Even the sounds of microscopic organisms only 50 microns in length could be recovered using a microscope and the techniques presented in the same reference.

In biomedicine, photoacoustic microscopy applies the photoacoustic effect to study certain tissue properties and reconstruct 2D or 3D images of target matter [10]. The photoacoustic effect as defined here relies on delivering some form of light into an area of interest which is then absorbed by human tissue. This absorption causes thermoelastic expansion and thus pressure wave propagation or ultrasonic emission. These emissions

can be captured and studied to derive various biological properties such as the tissue shape, oxygen saturation, or hemoglobin concentration [11]. In one application, photoacoustic imaging was used to reveal hidden underdrawings concealed in various artwork [12].

Any reliance on pressure wave propagation is lost for remote photoacoustic applications due to the lack of a transmission medium in the vacuum of space. However, one seemingly unresolved area of study is in the determination of an active form of remote sensing such as satellite laser ranging (SLR) that could be used to achieve a similar effect photoacoustic effect for RSOs. If an RSO of interest, potentially an inactive object of unknown material properties, could be pulsed with powerful enough SLR equipment, there may be a similar emission of energy somewhere on the electromagnetic spectrum. If it were possible to generate this electromagnetic energy emission and the signal-to-noise ratio (SNR) were adequate for either remote or satellite-to-satellite detection, it may be possible to derive RSO properties similar to how the photoacoustic effect is exploited in biomedicine. It seems reasonable to define this effort as remote laser photoacoustic spectroscopy, but further research is required to determine plausibility.

## APPLICATION TO SPACE SITUATIONAL AWARENESS

The direct application and benefit of photoacoustic sensing to Space Situational Awareness (SSA) efforts from a characterization standpoint is in deciphering what type of event occurred on-board an active satellite. While analyzing hypertemporal photometric data in the frequency domain may allow for the detection of an event, the frequency content alone is likely unable to correlate the detection to a physical event. The acoustic playback of an anomalous event should yield unique signatures that the human brain is capable of deciphering. Some common spacecraft events that may be detected

include the vibration induced by a solar panel deployment, scanning mirror operation during Earth imaging, antenna articulation, thruster ignition, momentum wheel desaturation, or other science instrument operation. Without any *a priori* knowledge of component operating profiles nor their frequency range, it becomes difficult to identify which spacecraft subsystem is activated by solely studying its photometric content. However, coupling the traditional frequency analysis with the acoustic representation of these spacecraft events should allow for the brain to differentiate between the sound of unique component functions like a thruster fire event compared to the articulation of an imaging system operating.

As previously stated, there are no external microphones in space and no methods to remotely capture acoustic sources occurring in space due to the lack of a transmission medium. One of the few known remote data sources that can be collected and used to create spectrograms in the human audible range is photometric data. Thus, a terrestrial analogy supporting the claim that acoustic signal perception allows for physical event correlation is illustrated in Fig 6. The difficulty in precisely determining the source of the signal in Fig. 6 becomes apparent while observing the spectrograms without any *a priori* information. Aside from a marine biologist, it is unlikely that one could deduce a Humpback whale produced the signals displayed in the spectrograms without any further context. Even as a zoological acoustics expert, signal identification could become difficult without comparison to a fully populated acoustic source library due to intraspecies variations.

An example that illustrates how two similar photometric profiles can handily reveal unique source events via acoustic playback is shown in Fig 7. From a power level, dead zone, profile, and spectral content perspective, both signals in Fig 7. are quite alike.

Similar to the Fig. 6 example, physical event correlation is difficult from a standalone spectrogram analysis.

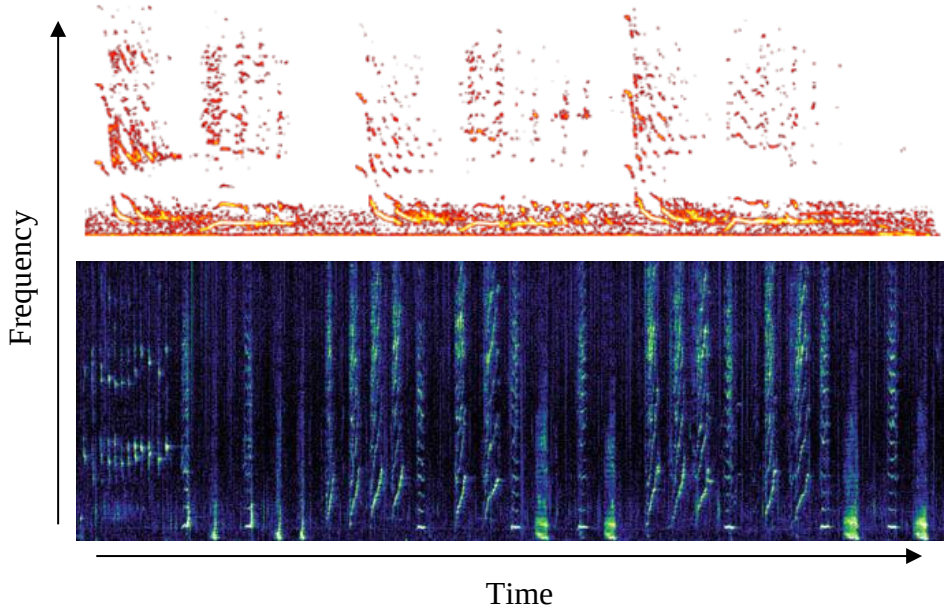


Figure 6: *(Top)* Spectrogram of the call of a *Megaptera novaeangliae*, more commonly known as a Humpback whale, lasting approximately fifteen seconds[5] and *(bottom)* another humpback whale recorded off the coast of Australia [13].

Performing an acoustic conversion on the Fig. 7 data would reveal that the top spectrogram represents the sound of an enthusiastic crowd cheering at a sporting event. The same process for the bottom signal produces the sounds of the Indian Ocean crashing against a shoreline. Therefore, the same challenge is noted when analyzing the spectrogram of a space event. The sample size of possible space domain event sources is likely smaller, but the need to uniquely identify each remains the same. Mapping the

[5] Voices in the Sea. *Humpback whale song*. Accessed via http://cetus.ucsd.edu/voicesinthesea_org/species/baleenWhales/humpback.html.

photometric data into the acoustic domain provides the insight necessary to do so. Development of a spacecraft subsystem level operational spectrogram and photoacoustic signature reference database would further support space event identification.

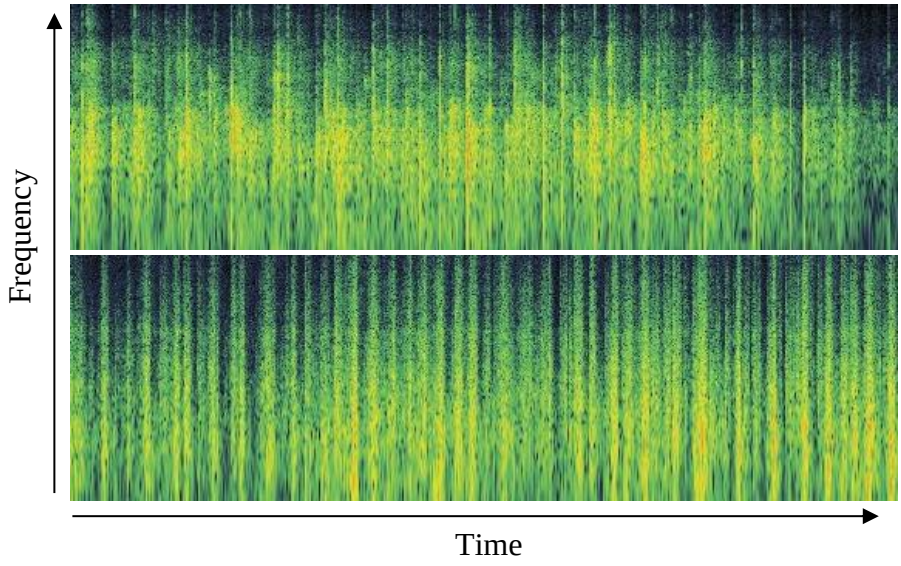


Figure 7: *(Top)* Spectrogram of a crowd cheering at a sporting event[6] and *(bottom)* another spectrogram of the Indian Ocean's waves crashing on a shoreline[7].

Like the Voyager 1 case study, the aural perception of any data can also give clues as to what or where to look in the frequency domain. This phenomenon is famously depicted by Hollywood in the movie Contact. When the character Dr. Clark listens closely to the acoustic interpretation of the anomalous signal coming from Vega, he detects a second signal embedded in the harmonics of the original solely by listening to its acoustic playback which clues the team in on what band to amplify and how to display it. While this exact depiction would not be realistic for the extraordinarily weak signals

[6] User qubodup. *Short Crowd Cheer*. Retrieved from https://freesound.org/people/qubodup/sounds/182571.
[7] User yurishkoda. *Indian ocean wave sound*. Retrieved from https://freesound.org/people/yurishkoda/sounds/125935.

the Search for Extraterrestrial Intelligence Institute scans for, the ability to naturally interpret a data set through sound remains a powerful tool.

It should be noted that the end goal of photoacoustic sensing is not to add "humans in the loop" at CSpOC or similar to continuously listen for all relevant active satellite events. This approach would be impractical for the scale of the SSA mission, although humans have been in the analysis loop for sonar detections in submarine warfare (e.g. acoustic differentiation of a depth charge, torpedo launch, or pod of whales). However, a one-off satellite-to-satellite observation may still be a practical application of real-time listening if a target satellite's behavior is of interest – potentially for mission characterization or diagnostic purposes. Once a certain physical event's origin has been determined, it is possible to begin training machine learning and pattern recognition algorithms to detect similar signals and associate them with certain RSOs or components such that the process could be automated. It may even become possible to predict satellite events by correlating pre-event frequency and photoacoustic content with future satellite behavior. Ultimately, implementing the human-machine interface required to train hypertemporal photometric data processing software is the first step in making remote photoacoustic sensing a plausible method for RSO event characterization and identification.

Acoustic interpretation further proves its worth when competing against the most advanced audio processing routines used today. There are challenges in differentiating between two humans speaking over each other, the sound of oceans versus a distant aircraft, and even snippets of music heard on the radio. These sorts of analysis require massive amounts of computational power and the latest technology is still chasing the brain [4]. Current audio processing algorithms operate by translating acoustic data into

some form of imagery, like the spectrogram, and then perform machine vision techniques to interpret it. Noisy auditory scenes and uneven phase cancellations across frequencies caused by similar tones make spectrogram analysis challenging [14]. At its core, machine vision is being used to perform machine hearing [15]. This method of processing audio is fundamentally different from how the human brain outright processes audio directly. Until audio processing algorithms advance past the brain's capabilities, perception of an event in the acoustic domain will remain a useful supplementary analysis tool.

### BIOMETRIC ANALYSIS

The same pattern recognition algorithms from the prior section could also begin to treat RSO event detections and nominal photometric profiles as biometric modalities that could be used to uniquely identify uncorrelated objects. Specific methods to accurately characterize photoacoustic signals are likely quite similar to how biometric recognition systems operate. The outgoing photon flux from any one RSO is dependent on object geometry, attitude, dynamics, and reflectance properties. Organizing the RSO event signal information into its unique frequency content, transients, pitch, aural perception, dead zones, harmonics, power level, profile, Mollweide projection, or other categories could provide the modalities necessary to implement a biometric recognition system. These biometric modalities fulfill the universality, distinctiveness, permanence, and collectability requirements for such a system [16][17]. The universality modality requires that each RSO exhibit a characteristic of interest. Distinctiveness enforces any two RSOs to be sufficiently different from each other in terms of the characteristic. Permanence is used in the sense that the characteristic should be invariant over a period of time. Finally, collectability necessitates that the particular characteristic can be measured quantitatively. Fusing these modalities with other known or inferred spacecraft parameters would yield

the equivalent of an n-factor authentication system regarding how to properly identify or "fingerprint" an RSO.

### INACTIVE RSO CHARACTERIZATION

The majority of the research herein studies active satellite characterization and event detection, but the concepts can and should additionally be applied to inactive objects. Remote photoacoustic sensing may provide an avenue to support inactive object characterization where current methods are lacking. One interesting case study could be to determine if a nominal vibration profile can be established for a discarded rocket body. Using inverse or regularization methods to develop a force profile as a function of time could yield useful insights. The ability to assess rocket body break up event hazards may correlate to the amount of residual fuel remaining. If the inactive RSO vibration profile were a function of residual fuel, there may be a method to gain these sorts of insights. If the regularization method proved useful enough to determine a forcing profile, one can consider if any shape, inertia tensor, or mass properties could be inferred. Likewise, the force profile could potentially support thrust profile definitions for active satellites.

It should be noted that while this research relies on visible wavelengths to study the frequency and acoustic content generated from RSOs, any energetic radiation could be used as an event sensing and characterization conduit. It is plausible that other electromagnetic emissions such as infrared, microwave, X-rays, radio, or ultraviolent spectral regions could be used.

# Chapter 4

# Active Satellite Event Detection

The prior sections discussed the potential for RSO event characterization and identification via acoustic interpretation of remote photoacoustic signatures obtained from active satellite observations. The satellite events assumed detection through either direct thruster plume observations for maneuvers, subtle changes detected in the hypertemporal photometric data frequency content due to an on-board event, or a combination of the two. This section will define specifics of the event recognition techniques from a satellite vibration mode change detection standpoint, focusing primarily on maneuvers. While the focus remains on propulsive events, these techniques could readily be applied to collision, explosive, or disintegration events and abrupt changes in the space environment.

## CURRENT STATE OF MANEUVER DETECTION TECHNIQUES

Methods to detect unmodeled dynamic events are often passive techniques that implement an algorithm to sample historical ephemeris data and perform statistical analysis until it can suggest an object's trajectory has shifted. Assuming the unmodeled dynamic event is a maneuver and depending on the magnitude of the burn, this sort of event detection can take approximately ninety minutes to several days to resolve. If the burn is small enough, it may be indistinguishable from natural perturbative effects [18]. Large maneuvers may cause a complete loss of an object's trajectory and can be tedious to reacquire.

An active maneuver detection simulation for a geosynchronous satellite using ideal ground-based angles only optical tracking and sequential estimation tools showed

that an in-track $\Delta v$ of 1.0 m/s could be detected as soon as fifteen minutes after a maneuver. A $\Delta v$ of 0.1 m/s was shown detectable in 6-12 hours and a $\Delta v$ of 0.01 m/s could take 12-24 hours or more to discern with confidence [19]. This simulation assumed a 250 m radial, 350 m cross-track, and 2,000 m in-track 1$\sigma$ *a priori* position uncertainty and two observation tracks per day. These techniques look at orbit determination measurement residuals with a defined threshold violation to indicate a maneuver has occurred. At the core of these methods is a detection lag as it takes more than a singular measurement to detect a trend, Mahalanobis outlier, or residual threshold violation. Kelcey et al. demonstrated that this lag is typically on the order of 2-3 days if using Two-Line Elements [20].

Patera demonstrated a maneuver detection technique using a moving window curve fit and achieved results similar to Kelcey et al. [21]. Some techniques such as in [22] apply optimal control theory metrics to constrain and solve for the control input. Hujsak shows that prediction of orbital elements or state vectors can be used to compare and evaluate if subsequent ephemerides correspond to natural propagation [23]. Yet another technique analyzes change in mechanical energy to estimate maneuver start and stop epochs without any *a priori* information via use of binary wavelet analysis [24].

Some techniques that employ traditional estimation techniques such as in [25] use optimization algorithms coupled with the admissible region to implement a batch least square fit on the thrust vector. Another approach by Lee et al. uses a Multiple Model framework and a bank of Extended Kalman Filters (EKFs) to model nonlinear jumps in the system [26]. Also, the ExoAnalytics data discussed in Chapter 2 demonstrate the possibility of direct event observations for large fuel dump and payload deployment events.

Aside from the ExoAnalytics case discussed previously, all maneuver detection techniques up to this point have been forensic methods – i.e. a detection is only made some time after the event has occurred. The advantage of utilizing photoacoustic sensing as an event detection paradigm is realized due to the methodology allowing for highly precise event epoch time stamping and direct observation of on-board anomalies that sufficiently excite detectable vibration modes. Assuming the target is captured and tracked within a telescope's FOV during a nighttime observation, two key factors that determine maneuver detection lag are the speed of light and data processing workflow. With modern computational power, this allows for a near instantaneous event detection capability. A comparison of prior techniques for a range of $\Delta v$ magnitudes is listed in Table 1.

| Detection Technique | Category | 1.0+ m/s | 0.1 m/s | 0.01 m/s |
|---|---|---|---|---|
| Statistical analysis of ephemeris data [18][20] | Passive | As early as 90 minutes, N x 90 multiples, days | As early as 90 minutes, usually days | Usually cannot detect |
| Angles only optical tracking [19] | Active | 15≤ minutes | 6-12 hours | 12-24+ hours |
| Electro-optical[4] | Passive / Active | Near real time | Unknown | Unknown |

Table 1: Comparison of current state of maneuver detection techniques.

## MANEUVER DETECTION VIA HYPERTEMPORAL PHOTOMETRY

The physical processes that make near instantaneous maneuver detection via remote photoacoustic sensing possible are as follows. The first step in a detection begins when a satellite activates its propulsion system and ignites its thrusters. The operation of a thruster assumes its initiation and nominal operation impart energy into the satellite body. This energy may induce vibration in flexible components or other structures depending on the geometry, material, and inertial properties of the satellite. If any of these structures have reflective surfaces, the reflected photon flux will be modulated by the induced vibration. Further, if the relative displacement of the reflective surfaces is large enough, it should be possible to detect the change in outgoing photon flux if the photometric data are collected by an optical telescope at a sufficient rate, optimally above 40 kHz.

This methodology provides a means to directly timestamp maneuvers and other operational events in space. With event epoch error bounds as large as a full orbital period demonstrated in some of the prior literature review, it becomes impossible to accurately estimate spacecraft parameters that involve any sort of time dependency with this technique. However, the direct event epoch observations via photoacoustic sensing can provide the ability to estimate impulse-related spacecraft parameters that were not possible with current techniques due to their large event epoch error bounds. While tracking the RSO throughout the entire event duration would support photoacoustic characterization efforts, only the initial and final event epochs require observability to allow for estimation of the parameters in the next two chapters.

To demonstrate a detection, a 2 kHz synthetic light curve is simulated for an active, 3-axis stabilized, nadir pointing satellite in GEO assuming a basic box-wing

structural model and a simplified Cook-Torrance reflectance model [27]. The light curve model was modified to operate on a flat-plate surface and relies on both diffuse and spectral bidirectional reflectance distribution function properties, incidence angles, and reflected intensity values [28]. To calculate the apparent visual magnitude as measured by an observer, the following formula can be implemented:

$$m_{v,object} = m_{v,sun} - 2.5log_{10}\left(\sum_{i=1}^{N_{facets}} \frac{S_i}{\rho_d^2}\right) \tag{1}$$

where the sum term denotes the effect from each given facet of the box-wing satellite model used. The intensity relative to the sun's apparent brightness generated from each facet and reflected in the direction of the observer is

$$S_i = \left(\frac{C_{d,i}}{\pi} + \frac{C_{s,i}}{\cos\theta_i}\right) A_i (N_i \cdot L)(N_i \cdot V) \tag{2}$$

and the incidence angle is defined simply by

$$\theta_i = \cos^{-1}[N_i \cdot L] \tag{3}$$

which is the angle between the facet surface unit normal vector and the unit vector from the sun to the RSO. The reflected light vector and relative surface angles are depicted in Fig. 8.

The simulation includes logic to determine which faces of the satellite are lit by the sun at any given moment, accounts for Earth eclipse, and has the ability to dynamically check for the proper mixture of diffuse and specular coefficients. The model does not account for any self-shadowing effects that may arise for a small subset of orbital geometries based on the simplified box-wing model orientation.

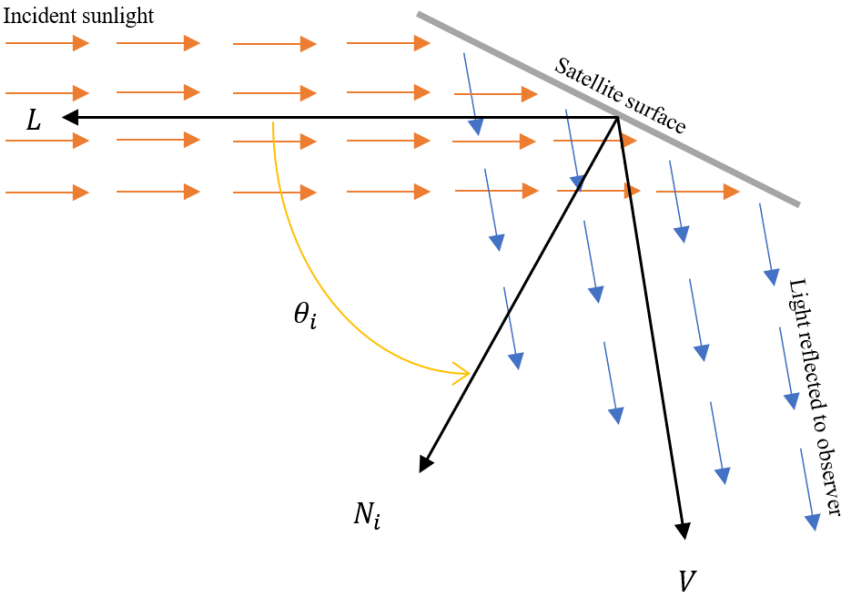


Figure 8: Illustration of the relative surface angles defined for use in the synthetic light curve simulation.

The 2 kHz value is chosen for computational run time reasons and to ensure at least a kilohertz order of magnitude post Nyquist Theory application is available for analysis. This 2 kHz rate also allows for realistic audio playback given the simulated event frequencies are at least two orders of magnitude below the sampling rate. The initial state is defined based on the known position of a telecommunications satellite provided by a willing operator who supported further collaborative efforts discussed in the future sections. Observability from the optical telescope used in acquiring experimental data in Chapter 7 is also a factor in choosing the initial state. All simulated light curves included an additive effect on the apparent visual magnitude induced by atmospheric turbulence. The effect is modeled as zero-mean, Gaussian distributed noise with a 0.04 $m_v$ standard deviation unless explicitly stated otherwise, also denoted as

$\mathcal{N}(0,0.04^2)$ in units of apparent visual magnitude ($m_v$). Other basic spacecraft parameters implemented in the simulation are listed in Table 2.

| Surface Area | Value | Material | $C_{d,i}$ | $C_{s,i}$ |
|---|---|---|---|---|
| +X / -X Face | 6 $m^2$ | MLI Kapton | 0.04 | 0.59 |
| +Y / -Y Face | 8 $m^2$ | MLI Kapton | 0.04 | 0.59 |
| +Z / -Z Face | 12 $m^2$ | White Paint / Germanium Kapton | 0.80 / 0.28 | 0.04 / 0.18 |
| Solar Panel | 15 $m^2$ | Solar Cells | 0.04 | 0.04 |

Table 2: Cook-Torrance model parameters used in generating a synthetic light curve.

To simulate a thruster fire event, a 58 Hz shear-like mode for the satellite bus and a clamped cantilever mode for the solar panel are induced as depicted in Fig. 9. A range of burn durations less than or equal to five seconds are investigated, a realistic value for collision avoidance maneuvers. The 58 Hz event frequency is chosen somewhat arbitrarily but mainly to avoid low frequency power observed in experimental data that could potentially obscure unique events. It appears that some active satellite vibration modes exist in the 3-12 Hz range based on on-orbit test data, but it will vary depending on mission requirements [28]. Other anecdotal evidence points towards active modes existing above 50 Hz for large Earth-imaging and weather satellites.

In general, the largest displacements will originate from the lowest mode frequencies, thus the 58 Hz source value is potentially overestimated if attempting to optimize event detection probability. However, the following conclusions remain the same as the simulations can be repeated with a lower frequency to produce the same results. The low frequency power associated with the zero hertz, direct current (DC) signal components has the potential to make distinguishing unique event correlation

peaks more difficult; however, experimental results discussed in Chapter 7 give confidence in the ability to maintain the same detection capability as the 58 Hz case.

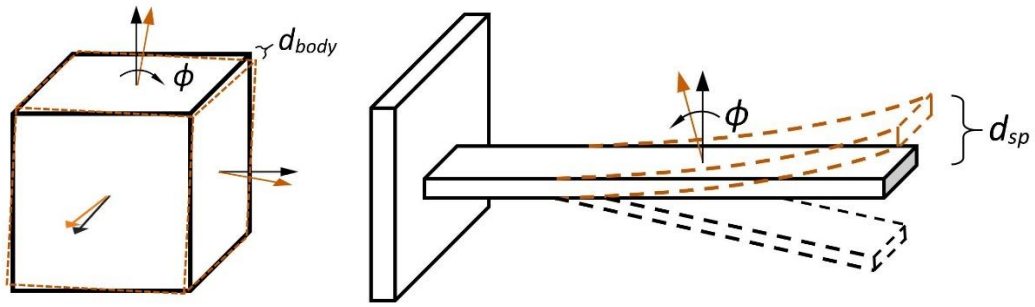


Figure 9: Illustration of the simplistic box-wing satellite vibration modes simulated.

Simulating the vibration mode is achieved by utilizing a simple oscillation model for the satellite bus and solar panel area unit normal vectors at the desired frequencies per Eq. (4) and Eq. (5) as follows:

$$\phi = \phi_{max} \sin[\omega(t - t_{burn})] \tag{4}$$

$$\hat{u}_{osc}(t) = R_n(\phi)\hat{u}_{srf}(t) \tag{5}$$

where $R_n(\phi)$ is the appropriate rotation matrix for a given satellite surface. It may appear as if the box model is undergoing a simple rotation, but the three faces not shown are rotated in the opposite direction, giving the shear effect as intended. It is assumed there is no complex deformation in the solar panel and thus the axis of rotation about the rigid wing model is defined at the clamped beam interface. The simulation attempts to emulate a visualization of common flat plate satellite modes illustrated in realistic vibration tests

conducted in the 0-64 Hz low frequency range[8]. A realistic three-dimensional surface deformation simulation can be used for an improved representation of a satellite's photometric event fingerprint. It seems reasonable that the differences between the simplistic model implemented herein and reality are on the same order of magnitude due to the relatively small displacements involved.

The displacement magnitudes for these vibration models are dependent on the material composition, structural geometry, and forcing function imparted by the thruster operation. Instead of building a macro model for a full fidelity structural vibration simulation, a range of displacement values are simulated such that a minimum detectable displacement threshold can be determined. The referenced displacement values are calculated as the peak or largest deflection at the extrema of the box face and solar panel surface areas respectively as defined in Eq. (6), Eq. (7), and Fig. 9.

$$d_{body} = \sin\phi \sqrt{\frac{A_z}{4}} \tag{6}$$

$$d_{sp} = \sin\phi \sqrt{A_{sp}} \tag{7}$$

The shear-like mode rotation point for the box model is defined on its respective area centerlines and is positioned at the hinge interface for the solar panel, hence the factor of four in the denominator of Eq. (6). It can be inferred that the shape of the solar panel is also a square in this case. The simulation assumes a step function for the thruster on and off events with no thrust profile effects included. An exponential and polynomial thrust profile were investigated but were shown to have negligible effects on detection

[8] Mode shapes retrieved from Olivier Dorival, *"Vibration tests on a satellite-like structure,"* 28 February 2011. Accessed via https://www.youtube.com/watch?v=dUewH84jNw8.

ability and event epoch definitions. The effects of a thrust profile should be considered on a case by case basis depending on the type of propulsion system as the margin for error around impulse duration is quite sensitive when estimating operational parameters in Chapter 6.

The results of a synthetic light curve test simulation are presented as follows in Fig. 10, with focus placed on both the noise-corrupted and reference signals.

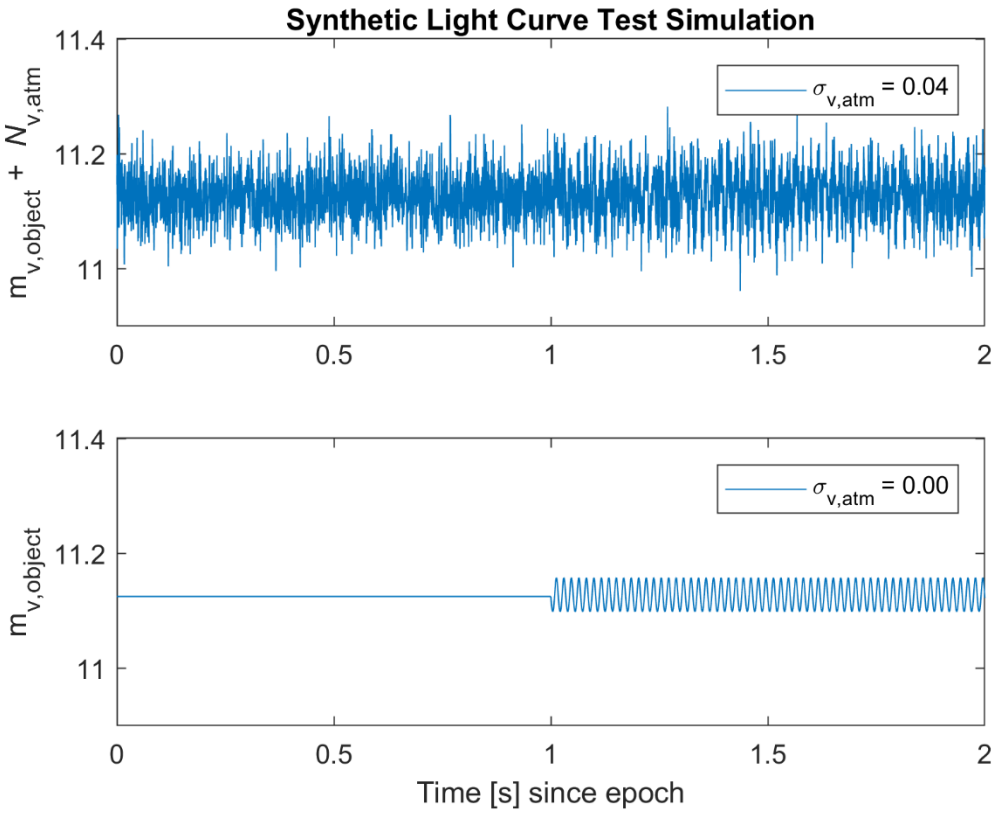


Figure 10: Apparent visual magnitude plots illustrating the reference signal with *(top)* and without *(bottom)* the effects of the atmospheric turbulence, to scale.

The +11.1 average apparent visual magnitude value seems reasonable for GEO distances assuming the reflectance properties defined in Table 1. The simulated maneuver and application of Eq. (4) and Eq. (5) begin at the 1.0 second since epoch tick mark. It may appear that the simulated event signal begins at a non-zero phase offset, but the asymmetry about the mean is due to the nonlinearities in the apparent visual magnitude calculation.

Without an *a priori* estimate as to which displacement value would produce a noticeable change in the light curve, an unrealistically large $d_{body}$ value of approximately 34 cm is chosen at an event frequency of 58 Hz. As seen in Fig. 11, this value is easily detectable through visual inspection of its spectrogram for a two second burn. The value is so large in fact that a 2N harmonic is present in the spectrogram. The large displacement likely begins to reveal parts of the neighboring satellite body surfaces which effectively doubles the fundamental frequency. On the leading and trailing edges of the signals displayed in Fig. 11, there exists a slight Gibbs-like phenomenon whose cause is likely due to the overlap, leakage, frequency resolution, and threshold values implemented in MATLAB's *pspectrum* function.

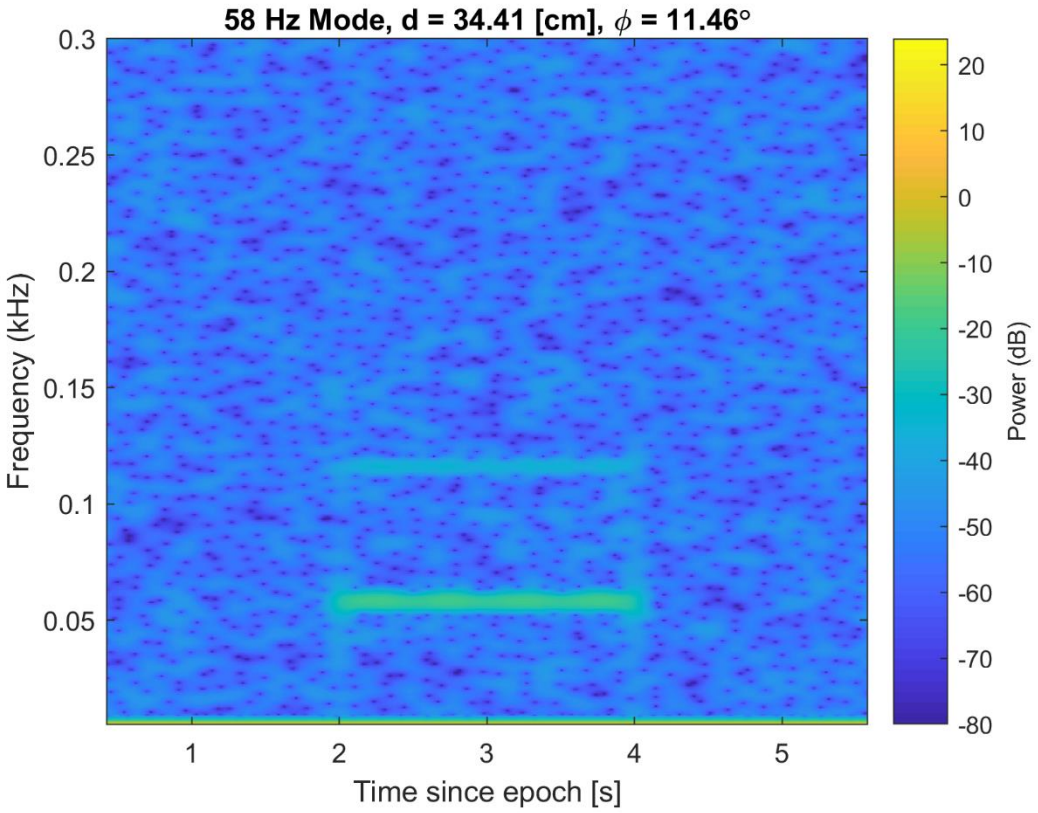


Figure 11: Spectrogram of a large displacement magnitude maneuver simulation.

Continuously decrementing displacement values through 8.70 cm, 3.46 cm, and finally 1.73 cm demonstrates the signal resolution reduction effect due the atmospheric turbulence. The 1.73 cm displacement case exhibits a loss of event signal detection to the atmospheric noise in Fig. 12, at least visually. In photometric data collection applications, it is generally uncommon to see atmospheric turbulence effects on the apparent visual magnitude standard deviations as high as 0.1-0.3 $m_v$, but it can occur. Standard deviations of 0.03-0.05 $m_v$ appear to be the best case for experimental optical data in industry [29]. The zero-mean, 0.04 $m_v$ standard deviation distribution is selected such that it is not overly optimistic and to represent industry leading optical equipment sensitivity.

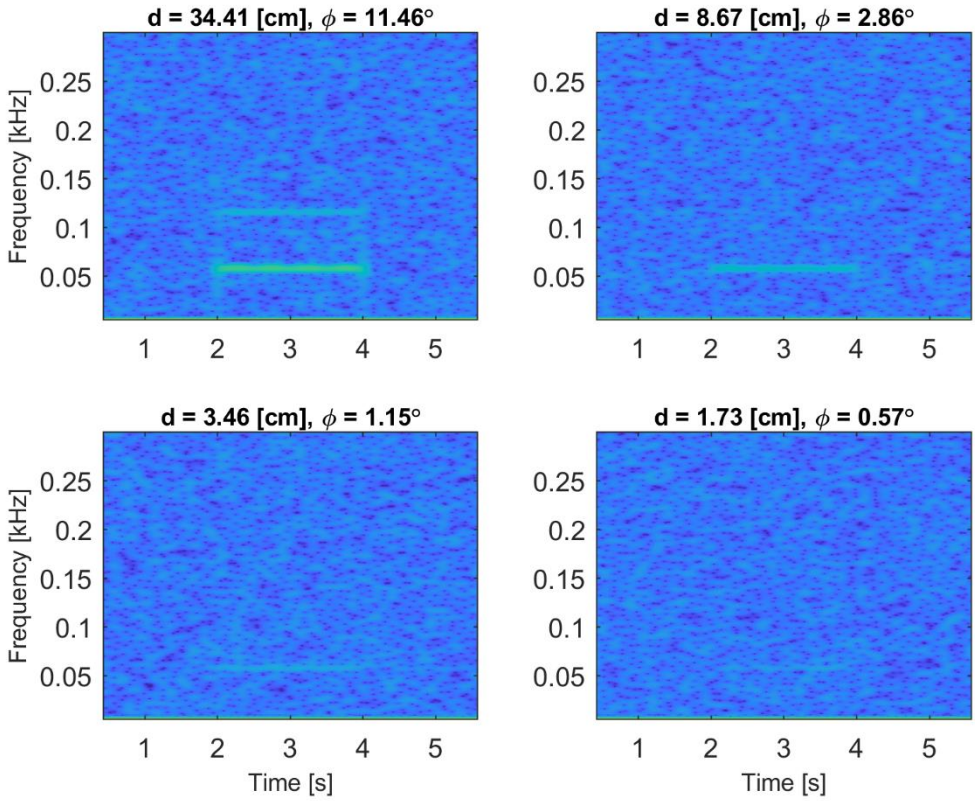


Figure 12: Spectrogram with decreasing displacement trend showing loss of visual signal detection at $d_{body}$ = 1.73 cm. Power scale is equivalent to Fig. 11.

Figure 11 and Fig. 12 assume maneuver detections via a change in satellite surface vibration modes in contrast to a direct thruster plume observation. The simulation produced an idealized, constant signal and thus the photoacoustic signatures are also of the same quality. The acoustic perception of the event can be described as a tonal hum as opposed to the more turbulent sound of a thruster plume in the Bloodhound SSC example. Again, the low-frequency tonal humming is expected as the source signal originates from the simulated structural vibration of the satellite body. The sound is comparable to a muffled, low rumble or mechanical apparatus such as a generator

operating at a low frequency. When attempting to characterize a thruster event from a pure body vibration standpoint, it may be more challenging than the case where a turbulent thruster plume is contained within the photometric content. It may be possible to derive thrust profiles from the spectrogram content. For instance, if the power magnitude for a particular signal is somewhat sinusoidal or depicts visual peaks, it could indicate a pulsing thruster usually associated with plasma or ion thruster classes.

### INFERRING SIGNALS FROM NOISE STRUCTURE

Considering all the assumptions made to produce the 3.46 cm displacement detection from induced satellite body vibration, the value is still relatively large. For a properly designed spacecraft, one would expect little to no relative structural motion. Thus, if an on-orbit experimental detection is to be made based on a change in relative surface displacements, small magnitude displacement detection capabilities are required. Aside from minimizing the effects of the atmospheric turbulence with adaptive optics and improving the signal-to-noise ratio, one method to improve the detection criteria and infer event signals from structure in the noise is to implement cross-correlation. Cross-correlation is a signal processing method that measures how similar two time series of data are as a function of relative phase offset. At its core, cross-correlation is a convolution of two functions, i.e.,

$$(f * g)(\tau) \triangleq \int_{-\infty}^{\infty} \overline{f(t)} g(t+\tau) dt \tag{8}$$

where $f$ and $g$ are the two signals and $\tau$ is the phase offset.

For the case of inferring an event signal present in low signal-to-noise ratio environments, the cross-correlation technique will need to be used in a sort of atypical

manner. The form of Eq. (8) is well prepared to compare two signals and determine at which phase lag exists the highest correlation; however, in this case the parameters of both signals are unknown. The range of possible values for vibrational mode frequency parameters is plausibly constrainable to the 0-100 Hz range based on knowledge of standard satellite structural design practices, yet the true event signal will remain unknown in an experimental data collection scenario. Thus, a reference signal must be selected, and the cross-correlation algorithm is to be applied across all possible frequency bands to determine which frequency displays maximum correlation and by what magnitude. In this manner, it should be possible to identify signals that exist as hidden structure in the apparent visual magnitude noise induced by the turbulent atmosphere.

Another exercise to demonstrate how cross-correlation will operate in this scenario is to imagine multiplying and summing discrete reference signal values of varying frequency with the random signal until one frequency produces a relatively large sum. This large value is generated because certain values in the signal that were once observed to be a random process happen to have the largest number of occasional peaks when the reference value has peaks, and minima where the reference also has minima. This is the essence of the cross-correlation technique employed herein – determining which signal is most similar to any transient content or structure in the randomness induced by the atmosphere. The structure of the custom search algorithm defined above in the time domain using a simple sinusoidal reference is illustrated in Fig. 13. The burn durations used in the synthetic light curve generation were never longer than 5.0 seconds

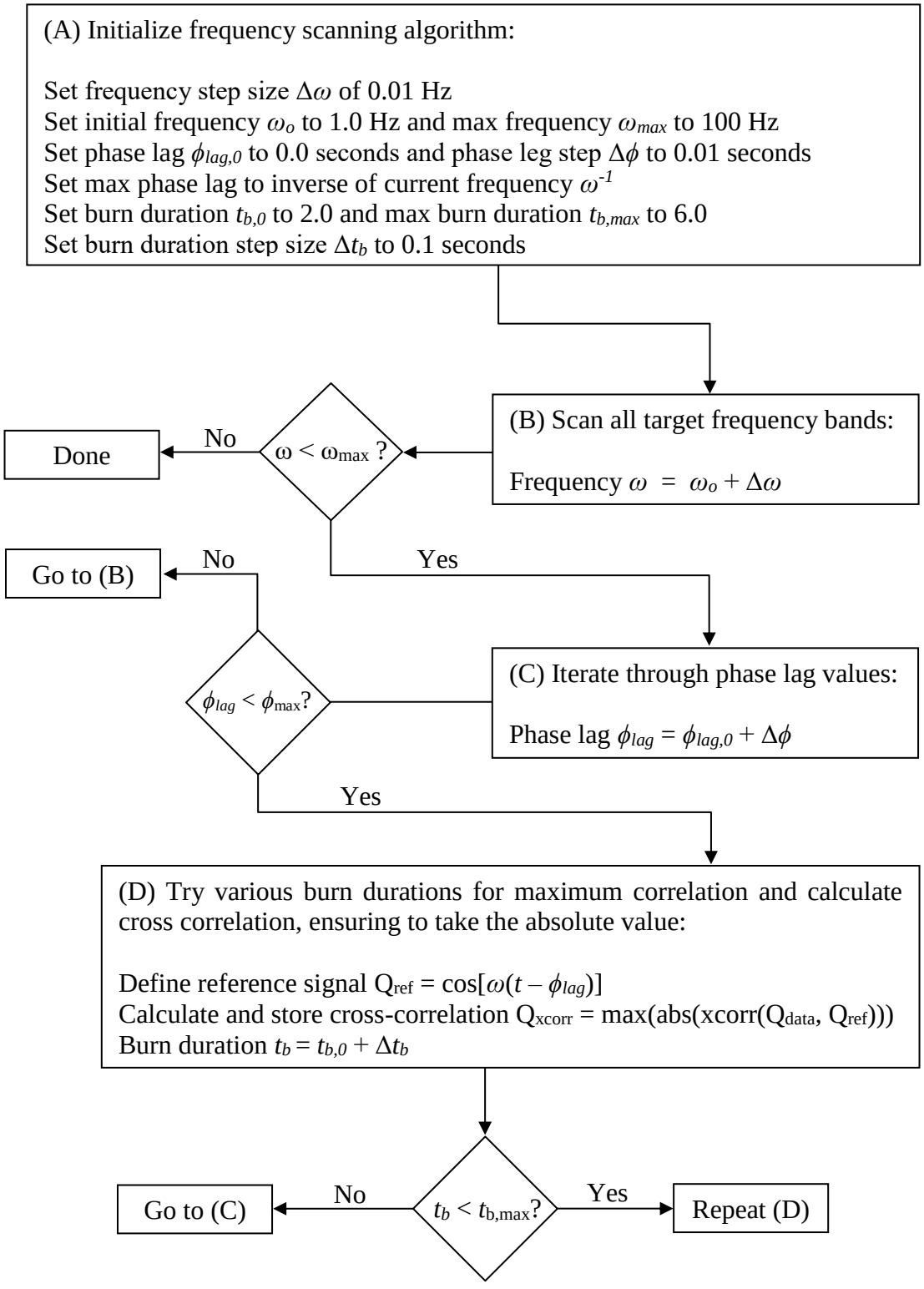


Figure 13: Flowchart of the custom signal search algorithm utilizing cross-correlation.

such that the scanning algorithm could be easily constrained. In an experimental scenario, the burn duration may need to be lengthened depending on the predicted maneuver duration. The algorithm in Fig. 13 also neglects the fact that the duration of the collected data may be much longer than any one particular window scanned at a given epoch. Thus, another layer of iteration using a moving data window throughout the entire time interval, defined as sections of $t$ in Fig. 13, must be added to properly search an entire collection of hypertemporal photometric data. Constraining all three scanned parameters to an optimally minimal region is ideal for computational reasons as scanning massive time and frequency bounds at a 50 kHz data rate all while performing a full numerical integration at each time step is a taxing operation on any central processing unit. Access to large scale supercomputing systems could provide a tangible solution to processing long duration or continuous data. *A priori* knowledge of the true event signal allowed a minimal scan region for the sake of demonstrating a result, as did the relatively low sample rate of 2 kHz.

To prove competence of the cross-correlation scanning algorithm with a known spectrogram detection case, the synthetic light curve data for the large 34.0 cm deflection test from Fig. 11 is input. The signal is large enough that it can be visually detected in a simple apparent magnitude versus time plot as in Fig. 14. The cross-correlation technique detects the event signal without any difficulty, again at 58 Hz as in Fig. 15. The general trend from high to low correlation values as frequency increases is due to the ever-present low frequency power, i.e. the direct current component, that exists in the experimental data correlating with the lowest frequency bands scanned. Searching for peaks should be constrained to finding local maxima, not global, as the relative-to-neighboring frequency correlation peaks are what is of interest.

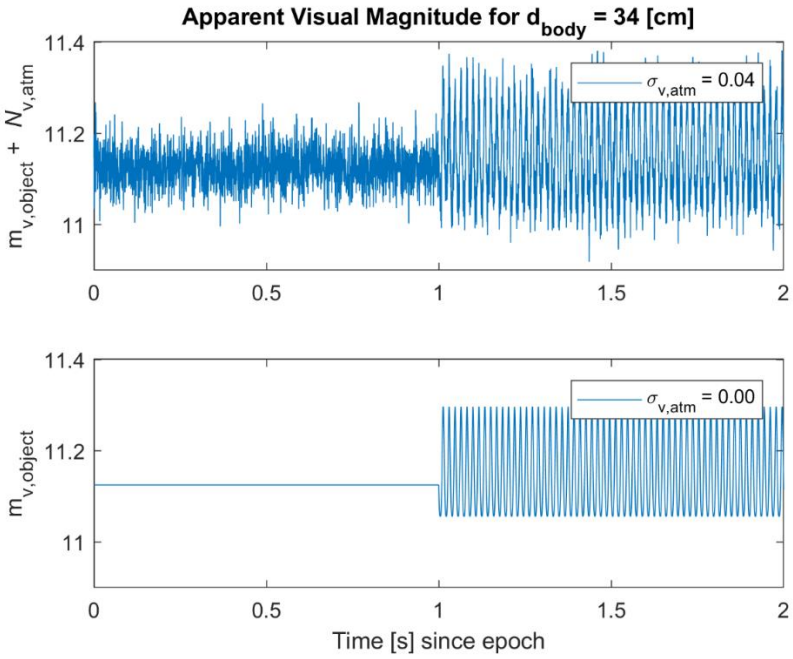


Figure 14: Apparent visual magnitude versus time for a large displacement test case.

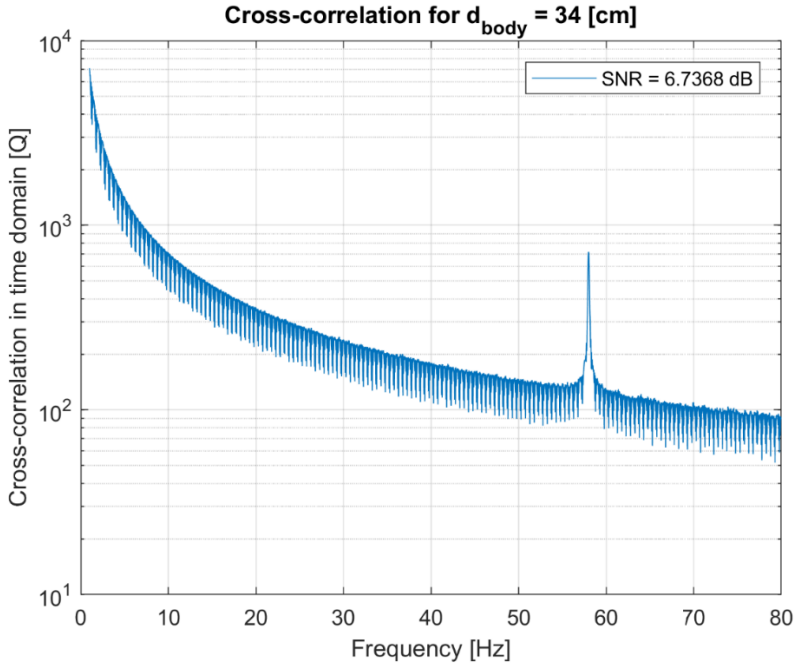


Figure 15: Cross-correlation of a large displacement test case demonstrating detection of a 58 Hz event signal as proof of concept.

Now that the cross-correlation scanning algorithm is proven for large signals, a more challenging search is performed. The previous minimum detectable displacement $d_{body}$ value from the standard spectrogram analysis was defined as 3.46 cm from Fig. 12. The results of implementing cross-correlation for the $d_{body}$ value of 1.73 cm where the signal was previously lost are displayed in Fig. 16.

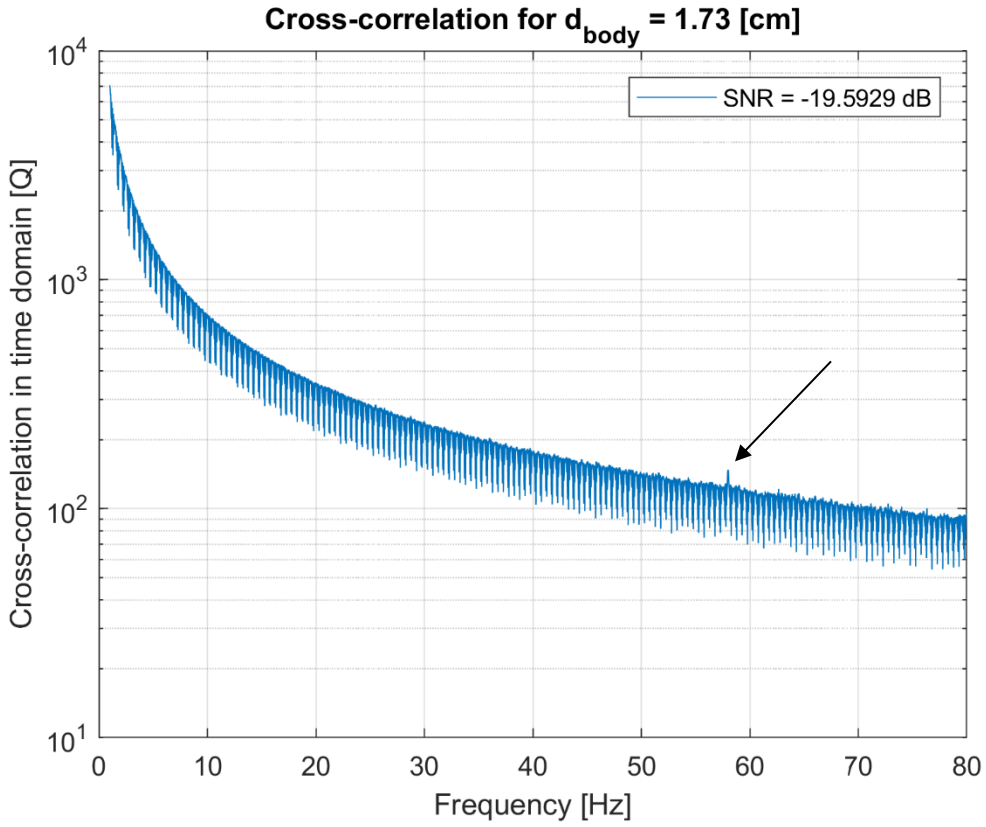


Figure 16: Cross-correlation results from the 1.73 cm displacement case showing event signal detection, again at 58 Hz as indicated by the arrow.

The technique is successful in detecting a peak at the 58 Hz event frequency, albeit a smaller peak. For comparison to the spectrogram analysis, a slightly different formulation of the short-time Fourier Transform (FFT) is performed on the same data,

also showing a detection at the same frequency in Fig. 17. To determine a lower bound on the displacement detection, decreasing values are continuously input until the cross-correlation algorithm is unable to confidently distinguish the event signal. The lower bound is determined to be a $d_{body}$ value of 7 mm from Eq. (6) for the body displacement as shown in Fig. 18. This calculation assumed the same noise distribution with a 0.04 $m_v$ standard deviation on the apparent visual magnitude calculation due to the turbulent atmosphere. The Fourier Transform method could not confidently distinguish from false peaks at this displacement magnitude as demonstrated in Fig. 19.

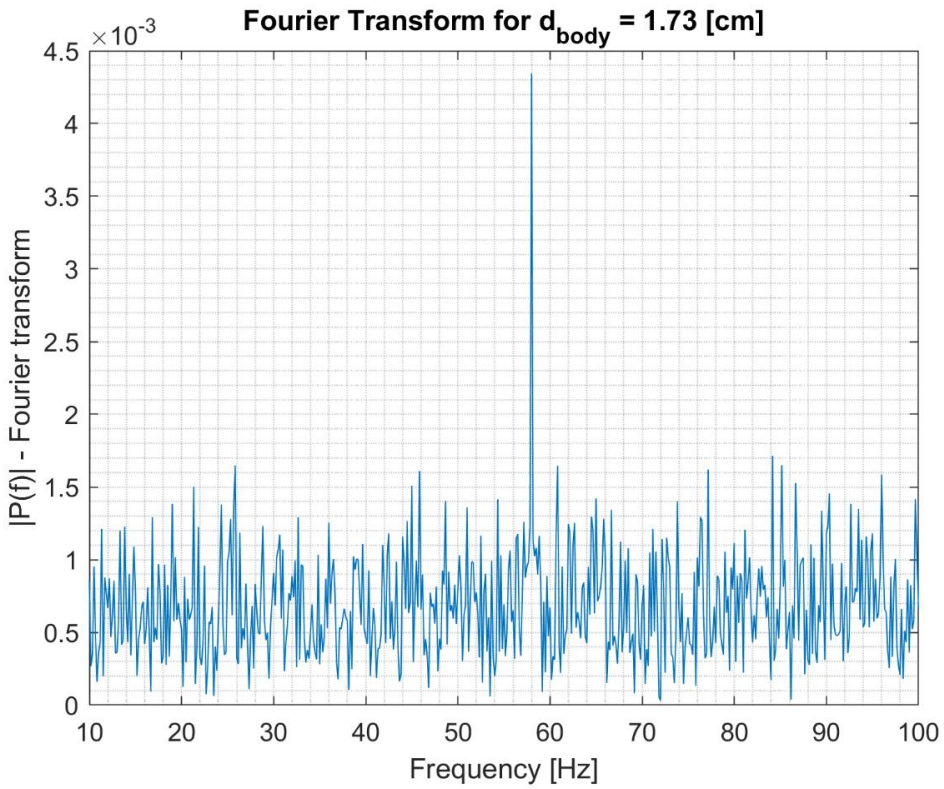


Figure 17: Fast Fourier Transform of the 1.73 cm displacement case also showing a detection at 58 Hz.

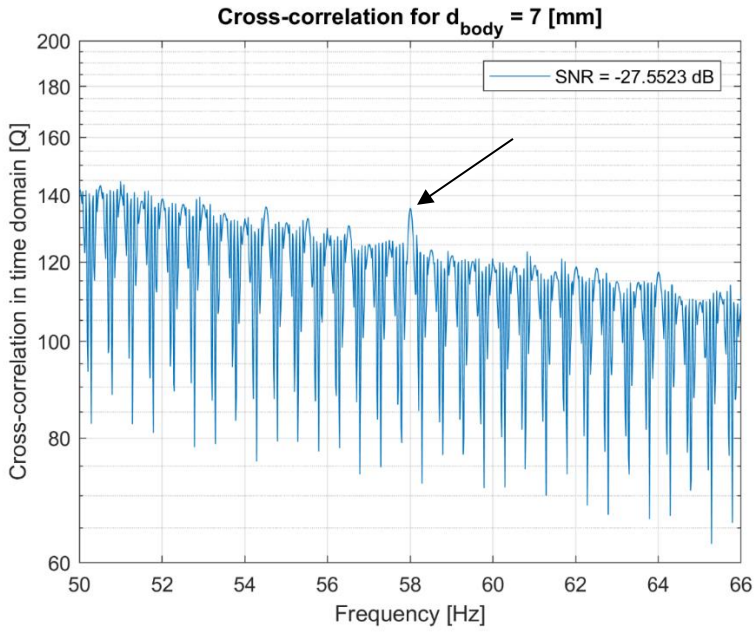


Figure 18: Cross-correlation results for the 7 mm lowest bound case with 0.04 $m_v$ standard deviation on the atmospheric noise, zoomed view.

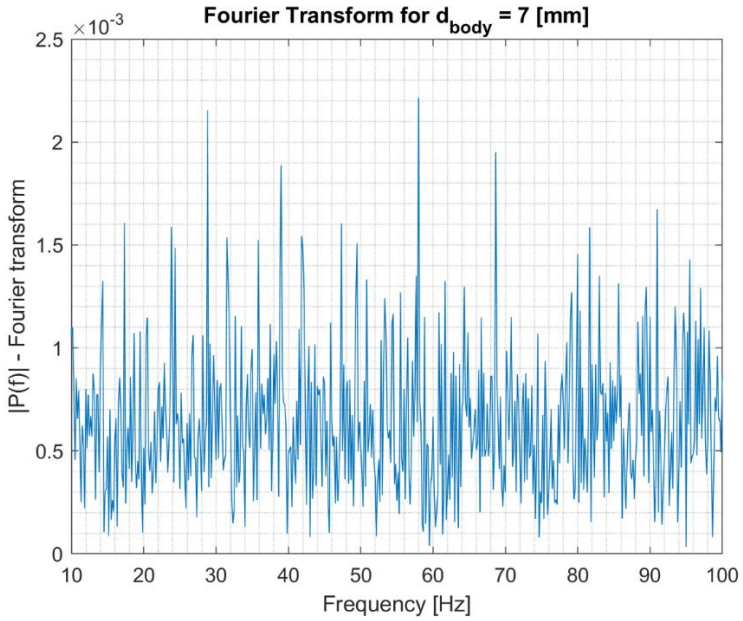


Figure 19: Fast Fourier Transform of the 7 mm lower bound case with 0.04 $m_v$ atmospheric noise standard deviation demonstrating that the FFT is unable to uniquely identify the 58 Hz event signal.

It is plausible the Fourier Transform is unable to singularly identify the event frequency due to algorithmic nuances. The base form of the Fourier Transform in Eq. (9) after generalization from the well-known Fourier series is a convolution like the cross-correlation, but the finite windowing effect that most FFT algorithms employ may have limited its resolution.

$$\hat{f}(\xi) = \int_{-\infty}^{\infty} f(x) e^{-2\pi i x \xi} dx \tag{9}$$

The cross-correlation algorithm can be implemented on a pre-Fourier transformed time series, but due to the same time-window limitations, only the native time series were input. The discussion of event detection suggests defining a relative cross-correlation peak threshold to determine when an event occurred. The research herein employed visual inspection of cross-correlation results or a relatively simple local maximum search algorithm to determine when an event had been detected. It would be worthwhile to develop a more rigorous statistical approach, potentially using outlier criteria.

Assuming a best case 0.03 $m_v$ standard deviation, zero-mean apparent visual magnitude distribution for the atmosphere-induced noise, the cross-correlation algorithm yielded an event detection lower bound of 5.2 mm for $d_{body}$ as shown in Fig. 20 and at scale in Fig. 21. This result demonstrates an approximate order of magnitude improvement from the prior best case lower bound of 3.46 cm.

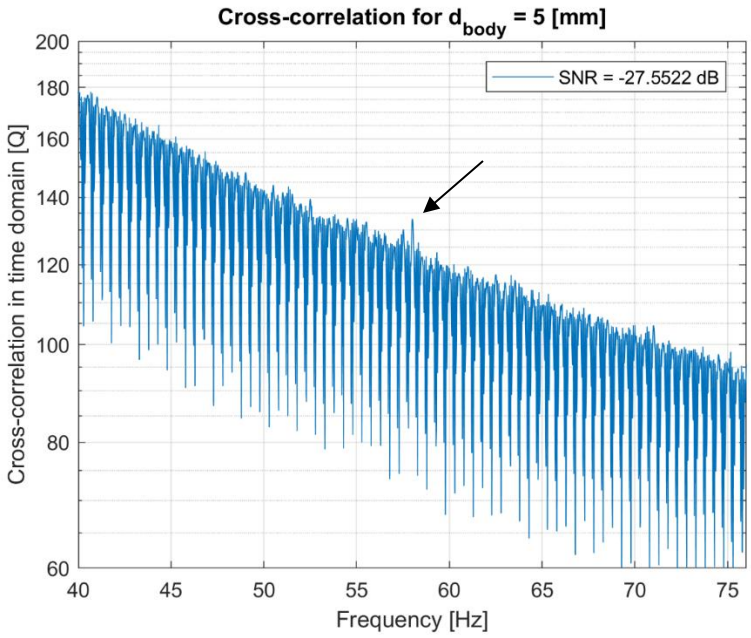


Figure 20: Cross-correlation of the 5.2 mm lowest detectable displacement case with a 0.03 $m_v$ atmospheric noise standard deviation, zoomed.

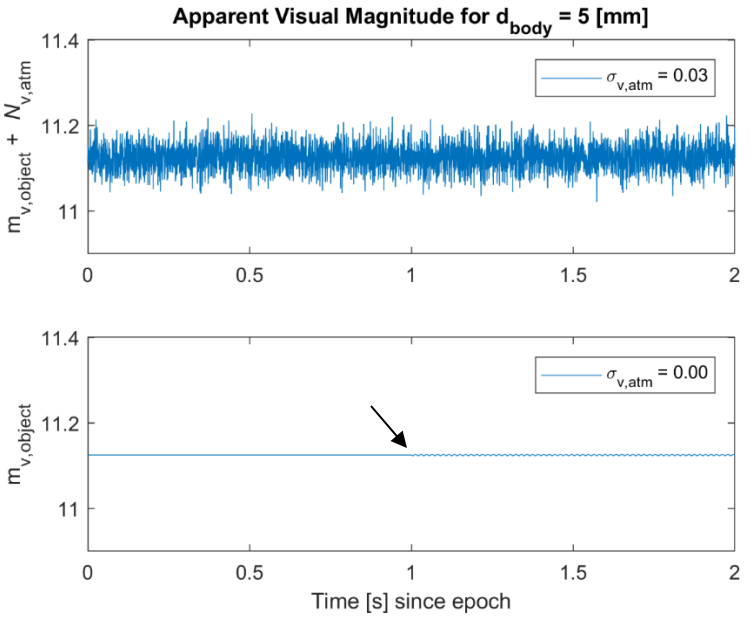


Figure 21: Apparent visual magnitude plots showing the relative signal-to-noise scales for the 5.2 mm displacement case with 0.03 $m_v$ atm. noise std. deviation.

The signal-to-noise ratio for the 5.2 mm detection case as well as the prior cases were calculated as in Eq. (10) in units of decibels and yielded the values in Table 3. The SNR for the minimum detectable displacement criteria for both the 0.03 $m_v$ and 0.04 $m_v$ noise standard deviation assumptions seemed to converge to the same value. This apparent convergence suggests there may be a lower bound on the SNR around -27.55 dB for event detection via cross-correlation. In the future, more simulations and SNR sensitivity studies can be performed to better constrain a useful detection lower bound.

$$SNR = 10 \log_{10} \frac{\sigma_{sig}^2}{\sigma_{v,atm}^2} \tag{10}$$

To reemphasize how the displacement magnitudes were calculated, it should be noted that the value $d_{body}$ and $d_{sp}$ were calculated at the furthest lever arm distance from the axis of rotation. Thus, much of the spacecraft body displacements contributing to the spacecraft event detection are much lower than the peak value. Throughout this research, it is assumed that the atmospheric noise randomness is the dominating factor in the ability to detect a potentially hidden event signal. If this were not the case due to some other aberration or instrument measurement noise, then these calculations must be reevaluated. However, it seems plausible that the randomness induced by the turbulent atmosphere is at least one order of magnitude larger than any randomness induced by a highly calibrated photon sensor or any other systematic error.

| $d_{body}$ | $d_{sp}$ | $\sigma_{v,atm}$ | SNR |
|---|---|---|---|
| 5.20 mm | 1.16 cm | 0.03 | -27.55 dB |
| 6.93 mm | 1.55 cm | 0.04 | -27.55 dB |
| 1.73 cm | 3.87 cm | 0.04 | -19.59 dB |
| 3.46 cm | 7.75 cm | 0.04 | -13.57 dB |
| 8.66 cm | 19.36 cm | 0.04 | -5.59 dB |
| 34.41 cm | 76.94 cm | 0.04 | +6.74 dB |

Table 3: Signal-to-noise ratio values corresponding to displacement magnitudes.

The simulated 5.2 mm detection magnitude claims to be an impressive result with the given assumptions and when considering the scale of the observation distances, relative velocities, and atmospheric uncertainty. Determining realistic on-orbit displacements has proven to be quite challenging due to the proprietary nature of such information. With the spacecraft areas and shapes assumed in this research, a 1.73-meter lever arm peak tip displacement of 5.2 mm seems like a realistic propulsive-event driven displacement magnitude. There exists proprietary evidence from industry colleagues of an operator-confirmed imaging subsystem operation detection at a LEO slant range for a weather satellite via similar hypertemporal photometric methods. Other anecdotal evidence exists in the form of unexplained structure in hypertemporal data from certain studies performed by the Air Force Research Lab at the megahertz level sampling rate. It seems likely that these events caused at least a 0.5-1.0 centimeter displacement or the optical systems used in those studies produced a better SNR compared to the simulated and experimental results presented in this research.

The logical next inquiry that arises is what the limiting detection factor would be if there were no atmospheric turbulence to limit the event signal detection threshold. An immediate application for such a scenario with no or less atmosphere is a satellite-to-

satellite observation at a geosynchronous orbital distance. It is plausible that the limiting factors in this case would solely be the target satellite reflectance properties and the optical equipment measurement sensitivity.

# Chapter 5

## Maneuver Estimation

For propulsive events, the ability to directly timestamp the impulse allows for precise estimation of $\Delta v$ magnitude, direction, and maneuver type. Although the focus of this chapter will be on active spacecraft maneuvers, the same techniques can be applied to outgassing or explosive events. In this context, near real time estimation will be defined as the time duration between the maneuver completion epoch and post maneuver state resolution. Thus, once the state of the RSO is resolved to a desired level of uncertainty post maneuver, the given parameters can be estimated. This method assumes the detection of an event triggers active collection of data or sensor tasking to resolve the RSO's new trajectory after the maneuver.

The initial goal of this research is to collect experimental data on a satellite in GEO to confirm event detectability and prediction of maneuver parameters in near real time. Satellite operators at Optus, an Australian telecommunications company, were kind enough to provide states before and after station keeping maneuvers for various satellites in their constellation. Initial and final maneuver event epochs were provided such that any estimated values can be compared to well established reference data for each event. Thus, for the $\Delta v$ and any other spacecraft parameter estimation simulations, the initial satellite state for the following simulations used the operator-provided state in GEO, propagated to the initial event epoch. Any observation models and orbit determination studies of convergence time discussed were conducted in the LEO regime due to prior availability of fully validated observation schemes and measurement data. The following sections will describe the simulation and assumptions used to estimate $\Delta v$ magnitude, direction, and maneuver type in near real time.

**OBSERVATIONS**

The following simulations assume the target RSO is well tracked, appropriately tasked, and the state solution has converged. The satellite initial conditions define a non-inclined, circular orbit at a 790 km altitude. Apparent range and range-rate data utilized 10-60 second data intervals. The measurement site locations are assumed to be known within one meter and with no biases present. Arecibo was considered as a ground site and is used in validating the observation model but ultimately is not utilized in any convergence studies based on simulation time frames and the RSO orbital period. The convergence time studies assume a large measurement gap between stations to inject operational realism into the simulation. The Mt. Stromlo site location used in Chapter 7 is included in Table 4 for reference.

| No. | Description | $X_s$ [m] | $Y_s$ [m] | $Z_s$ [m] | Range $\sigma$ [m] | Range-rate $\sigma$ [mm/s] |
|---|---|---|---|---|---|---|
| 1 | Kwajalein Atoll | -6143584 | 1364250 | 1033743 | 10 | 0.5 |
| 2 | Diego Garcia | 1907295 | 6030810 | -817119 | 5 | 1 |
| 3 | Arecibo | 2390310 | -5564341 | 1994578 | 10 | 0.5 |
| 4 | Mt. Stromlo | -4467063 | 2683034 | -3667007 | 10 | 1 |

Table 4: Observation site locations and assumed measurement uncertainty.

The reference epoch values given from Optus were UTC time stamps accurate to microsecond precision. The GEO observations discussed in Chapter 7 have not yielded any direct experimental observations of maneuvers yet, although some anomalous LEO events for other spacecraft are still being studied. Thus, any estimation involving event timestamps used the operator-delivered reference or “truth” for simulation. Studies on

parameter estimation sensitivity are conducted to 0.5 seconds before and after the reference epochs and are presented in the $\Delta v$ estimation section.

The simulated data includes the effects of light time and is accounted for by propagating the satellite state to each observation time step minus the light time correction as per Eq. (11). Corrections were typically on the order of 20-75 meters for the LEO regime.

$$t_{l,c} = t_{l,a} - \frac{\rho_a}{c} \tag{11}$$

The observation model itself for apparent range and range-rate is defined in Eq. (12) and Eq. (13). It should be noted that the range rate equation does not include a range bias term in it as the time rate of change goes to zero for the range bias term when differentiating. It is also assumed the observation sites are stationary, i.e. no continental drift considerations were required for the time scales in this study.

$$\rho_a = \sqrt{(x - X_s)^2 + (y - Y_s)^2 + (z - Z_s)^2} + \rho_b \tag{12}$$

$$\dot{\rho}_a = \frac{(x - X_s)(\dot{x} - \dot{X}_s) + (y - Y_s)(\dot{y} - \dot{Y}_s) + (z - Z_s)(\dot{z} - \dot{Z}_s)}{\sqrt{(x - X_s)^2 + (y - Y_s)^2 + (z - Z_s)^2}} \tag{13}$$

**REFERENCE FRAMES**

All simulations are conducted in the Earth Centered Inertial (ECI) frame while site locations and observations are given in the Earth Centered Earth Fixed (ECEF or ITRF) frame. A complex Earth rotation model is used to transform between ECI and

ECEF, specifically the IAU-76/FK5 system using the J2000 epoch [30]. This system uses the IAU-1980 Theory of Nutation, IAU-1976 Precession Model, and includes polar motion. The precise rotation sequences are included below in Eqs. (14-16).

$$r_{ECI} = [P(t)][N(t)][R(t)][W(t)]r_{ECEF} \tag{14}$$

$$v_{ECI} = [P(t)][N(t)][R(t)][[W(t)]v_{ECEF} + \omega_E \times [W(t)]r_{ECEF}] \tag{15}$$

$$a_{ECI} = [P(t)][N(t)][R(t)][W(t)]a_{ECEF} \tag{16}$$

An important detail to note when transforming accelerations from ECEF to ECI for use in gravity models assumes any Coriolis and centripetal terms in the rotation are not included. Also, the Earth orientation parameters obtained from the International Earth Rotation and Reference Systems Service website are updated daily for all calculations [31]. To increase accuracy and limit any jumps in data between days, a cubic spline or similar technique can be used to interpolate values.

**DYNAMIC MODEL**

An accurate representation of the space environment dynamics is necessary to propagate orbital trajectories and uncertainty. It is assumed the satellite is 3-axis stabilized, nadir pointing, and any maneuver events were executed perfectly. The gravitational and non-gravitational forces assumed to be acting on the satellite are

gravity, lunar perturbations, solar perturbations, solar radiation pressure (SRP), and atmospheric drag.

The gravitational model implemented is the EGM-96 20x20 spherical harmonics model given in the Aerospace Toolbox in MATLAB [32]. The default code is streamlined and further optimized for run time considerations. This model computes the acceleration due to the non-spherical Earth, stated in the form of the gravitational potential energy in Eq. (17). The potential energy formulation is used in its direct form in Chapter 6, but to find the components of acceleration, the gradient must be calculated.

$$U_E = \frac{\mu}{r}\left[1 + \sum_{l=2}^{\infty}\sum_{m=0}^{l}\left[\frac{R_E}{r}\right]^l P_{l,m}\left(sin\,\phi_{gc_{sat}}\right)\left(C_{l,m}\,cos\,m\lambda_{sat} + S_{l,m}\,sin\,m\lambda_{sat}\right)\right] \quad (17)$$

Third-body perturbations due to the moon and sun are included in the force model. The simplified equations driving this effect are listed in Eqs. (18) and (19). The Astronomical Almanac has a simple algorithm available to calculate the position of the sun and moon relative to the Earth [33]. Caution should be taken in how one defines the spacecraft-third body vector relative to the Earth as the sign conventions and unit vector directions can easily be calculated incorrectly. For an increased fidelity planetary ephemerides representation, the JPL SPICE toolkit can be implemented.

$$\bar{a}_{3,sun} = \mu_{sun}\left[\frac{\bar{r}_{sat,sun}}{r^3_{sat,sun}} - \frac{\bar{r}_{Earth,sun}}{r^3_{Earth,sun}}\right] \quad (18)$$

$$\bar{a}_{3,moon} = \mu_{moon}\left[\frac{\bar{r}_{sat,moon}}{r^3_{sat,moon}} - \frac{\bar{r}_{Earth,moon}}{r^3_{Earth,moon}}\right] \tag{19}$$

A full facet-based, attitude dependent solar radiation pressure model corresponding to the six-dimensional cube shape of the box-wing satellite model and the solar panel is implemented according to the model in Eq. (20). It is assumed that the solar panel is double gimbaled and thus is always sun pointing. To find the unit normal vectors for each face of the spacecraft, a direction cosine matrix is implemented that incorporates the radial, in-track, and cross-track vectors. In addition to the facet-based model, a simple cylindrical Earth shadow model based on an ellipsoidal Earth is implemented. The solar panel faces themselves also require a logic to determine which faces are lit by the sun at any given time.

$$\bar{a}_{SRP} = -\sum_{i=1} \frac{p_{srp} A_i \cos\phi_{inc_i}}{m}\left[2\left(\frac{C_{d_i}}{3} + C_{s_i}\cos\phi_{inc_i}\right)\hat{n} + \left(1 - C_{s_i}\right)\hat{s}\right] \tag{20}$$

An exponential density model is used along with a velocity vector defined relative to the rotating atmosphere. The flight path angle is accounted for relative to the in-track face even though the orbit is near circular. It is assumed that the solar panel is included in the facet-based drag model, but no self-shadowing effect is considered. The specific form of each drag term is represented in Eq. (21) and Eq. (22).

$$\bar{a}_{drag,X} = -\frac{1}{2}\frac{C_D A_x \cos(\phi_{fpa})\rho v_{rel}\bar{v}_{rel}}{m} \tag{21}$$

$$\bar{a}_{drag,sp} = -\frac{1}{2} q \frac{C_D A_{sp} \cos(\phi_{v\_sun}) \rho v_{rel} \bar{v}_{rel}}{m} \tag{22}$$

The q term included in the acceleration due to drag imparted by the solar panel is simply a quadrant check with a value of -1 or 1 depending on the sign of the cosine term. Drag due to the main +X face of the satellite box-wing model should also have a quadrant check but because the orbit is near circular there is no realistic possibility for the flight path and in-track directions to be greater than 90 degrees. The flight path angle, incident angle between the solar panel and the velocity unit vector, and all other similar incident angles computed in the solar radiation pressure model are determined using the dot product-cosine relation for any two vectors in three-dimensional space.

### FORCE MODEL VALIDATION

To verify the force model developed is accurate, it is common practice to compare results over different propagation scenarios with other software suites, versions of force models, or formulations to guarantee consistency. A publicly available space mission design and navigation suite developed by the NASA Goddard Space Flight Center called the General Mission Analysis Tool (GMAT) is used to perform independent verification and validation in this scenario [34]. Implementing the same initial conditions and a range of force model fidelities as well as various propagation intervals yields the results in Table 5 and Table 6.

| GMAT Model | Position Difference [m] | Velocity Difference [cm/s] |
|---|---|---|
| 20x20 | 0.254 | 0.0264 |
| 20x20 + Lunisolar | 0.802 | 0.0802 |
| 20x20 + Lunisolar + Drag | 12.561 | 1.3188 |
| 20x20 + Lunisolar + Drag + SRP | 12.921 | 1.3545 |

Table 5: State error compared to GMAT propagation after six hours.

Over six hours, the force model agrees with GMAT to within 13 meters in position error. The main source of error seems to be the addition of drag. This intuitively makes sense as GMAT uses a Jacchia-Roberts density model which is considered more accurate than the simple exponential model implemented in this research. The propagation results agreed closely with the GMAT gravity field results.

| GMAT Model | Position Difference [m] | Velocity Difference [cm/s] |
|---|---|---|
| 20x20 + Lunisolar | 3.150 | 0.3440 |
| 20x20 + Lunisolar + Drag + SRP | 188.821 | 20.022 |
| 20x20 with RK89 propagator | 1.017 | 0.1070 |

Table 6: State error compared to GMAT propagation after 24 hours.

The position error after the 24-hour propagation cause is approximately what is expected for the gravity and luni-solar cases. The addition of drag and SRP start to cause divergence more so than the six-hour propagation, which is again due to the difference in drag models and spacecraft shape modeling. Accounting for the difference in drag modeling shows strong agreement in force models and thus stands to validate the dynamics used in this research.

## ORBIT DETERMINATION

The satellite's state post-maneuver, ballistic coefficient, and solar coefficient-area-mass combination are required to estimate $\Delta v$ parameters. The ballistic and solar coefficients can be assumed known based on the assumption that the RSO is well tracked and an estimation scheme similar to how CSpOC provides their coefficient estimates in conjunction data messages is implemented [35]. What sets photoacoustic sensing apart from other maneuver detection and estimation techniques is that it immediately allows for direct association of state measurements to old, new, or mid-maneuver arcs. This immediate association is possible due to the assumption that with photoacoustic sensing, the initial and final event epochs are observable and detectable via the hypertemporal photometric data analysis techniques presented in Chapter 4. Thus, any state measurements can be assigned either a pre-, post-, or mid-event designation based on the known event epochs. This allows for measurements post-maneuver to be treated as a new arc. Per the prior assumption that a sensor will actively begin collecting measurements on the satellite after event termination, state resolution of the RSO through traditional orbit determination methods using the post-maneuver arc measurements can be implemented. With emphasis on near real time estimation timelines, prediction of $\Delta v$ and any impulse related parameters become possible as soon as the satellite's position and velocity are known to a desired level of uncertainty post-maneuver.

Given the orbital regime, likely maneuver type, burn duration, and *a priori* uncertainty, it is possible to put forth an educated guess for the *a priori* covariance matrix utilized for the post-maneuver arc orbit determination. The pre-maneuver solution is assumed to have an accurate *a priori* uncertainty defined as a 10-meter 3σ covariance bound. Using this information, the *a priori* covariance matrix is formed as purely

diagonal with a 4.0 $km^2$ position variance and a 4.0 $m^2/s^2$ variance for the velocity components. As for the initial state estimate post-maneuver, perturbed position values ranging from 0.2 km to 5.0 km in all directions from the given reference state at maneuver termination are tested. Velocity offsets were also tested, but their effect on the orbit determination solution is negligible. The initial state offset is relatively easy to constrain given the pre-maneuver arc, but this effort can increase in difficulty for longer duration, non-impulsive burns.

Due to its current state nature and nominal trajectory update at each measurement step, an Extended Kalman Filter is chosen to process the post-maneuver measurements [36]. The real time updates of the state within the EKF align well with the desired near real time estimation. The EKF operates like a traditional Kalman Filter in that it linearly propagates the covariances as in Eq. (23) using the state transition matrix and additive process noise. The state noise compensation formulation utilizes a process noise transition matrix to provide a measurement gap dependency to the information.

$$\bar{P}_k = \phi(t_k, t_{k-1}) P_{k-1} \phi^T(t_k, t_{k-1}) + \Gamma(t_k, t_{k-1}) Q_{k-1} \Gamma^T(t_k, t_{k-1}) \tag{23}$$

To propagate the state transition matrix, the standard dynamic model $A$ matrix is utilized. For the $A$ matrix calculation, gravity partials up to the $J_4$ zonal term are included and only the solar panel portion of the SRP partials are used for computational run time reasons. The measurement mapping $H$ matrix is also calculated and both itself and the $A$ matrix are formed using MATLAB's Symbolic Toolbox. The familiar measurement update step is calculated using the innovations covariance from Eq. (24), Kalman gain from Eq. (25), and final state update as in Eq. (26).

$$P_{zz} = H_k \bar{P}_k H_k^T + R_k \tag{24}$$

$$K_k = \bar{P}_k H_k^T P_{zz}^{-1} \tag{25}$$

$$\hat{x}_k = \bar{x}_k + K_k(z_k - H_k \bar{x}_k) \tag{26}$$

A more numerically stable version of the covariance update using the Joseph Formulation is implemented as in Eq. (27).

$$P_k = (I - K_k H_k)\bar{P}_k(I - K_k H_k)^T + K_k R_k K_k^T \tag{27}$$

The EKF requires eleven observations at sixty second measurement intervals over a span of 29 minutes to achieve a 10-meter 3σ state uncertainty post maneuver as indicated in Fig. 22. The 29-minute span included a 17-minute measurement gap before the satellite is viewable by the next station. Using a ten second measurement frequency did not improve convergence time. It seems that for this orbital altitude, the uncertainty convergence is sensitive to observation consistency and station geometry. Assuming consistent measurements, priority tasking, and ideal station coverage, it also seems plausible that the uncertainty convergence time can be improved to near ten minutes.

For the same simulation, the measurement residuals and innovations covariance can give clues about solution stability. While stable measurement residuals do not always necessitate an accurate orbit determination solution, the residuals can be used as a first order indication that a filter's state estimate has converged. To study this behavior, the EKF post-fit range residuals and 3σ innovations covariance bounds are plotted in Fig. 23 to determine if any initial filter convergence epochs can be defined.

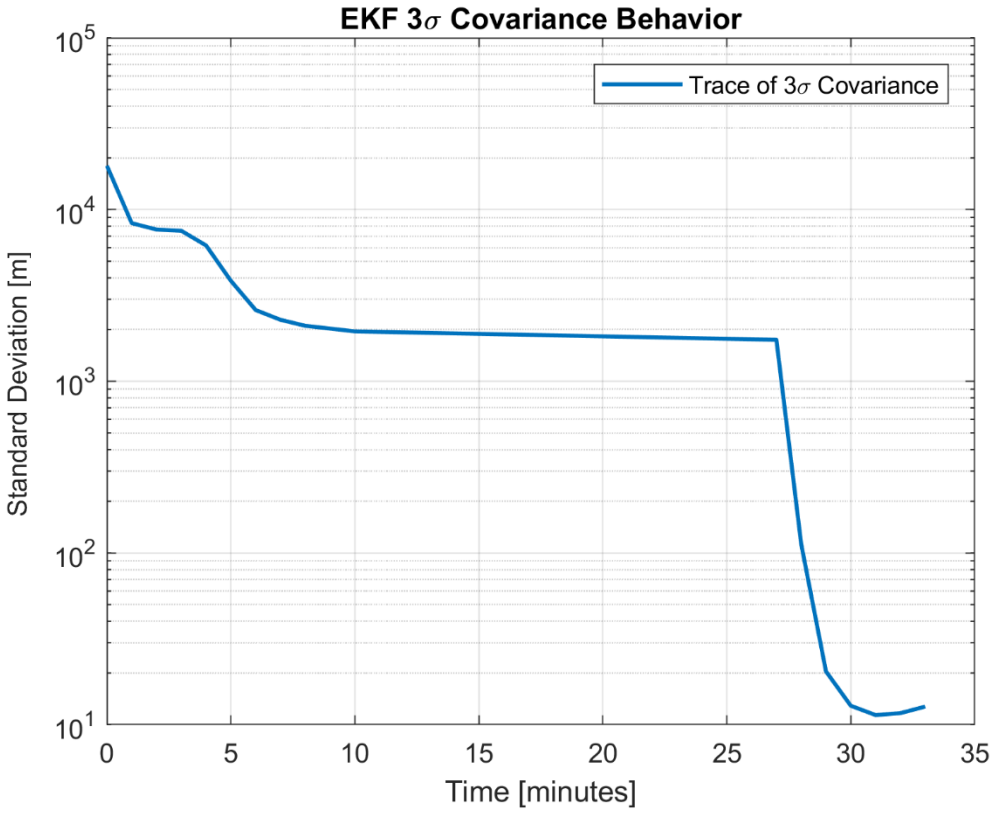


Figure 22: RSO post-fit state 3σ standard deviation value convergence over time. Note the acquisition of the Kwajalein Atoll sensor at 27-minutes after the 17-minute measurement gap causing an apparent discontinuity – this is simply due to new measurements reducing uncertainty.

After only two measurements, the range residuals have stabilized for the first station and the 3σ innovations covariance has achieved a steady 20-meter value. Thus, it seems generally plausible to estimate Table 7 and 8 parameters within five minutes of an active satellite maneuver using this technique and related assumptions. The accuracy of the estimated parameters discussed in coming sections demonstrates the innovations covariance convergence approximation technique is plausible. The near real time, five-minute estimation lag is credited to the direct event epoch time stamp observations made possible by the remote photoacoustic sensing event detection technique.

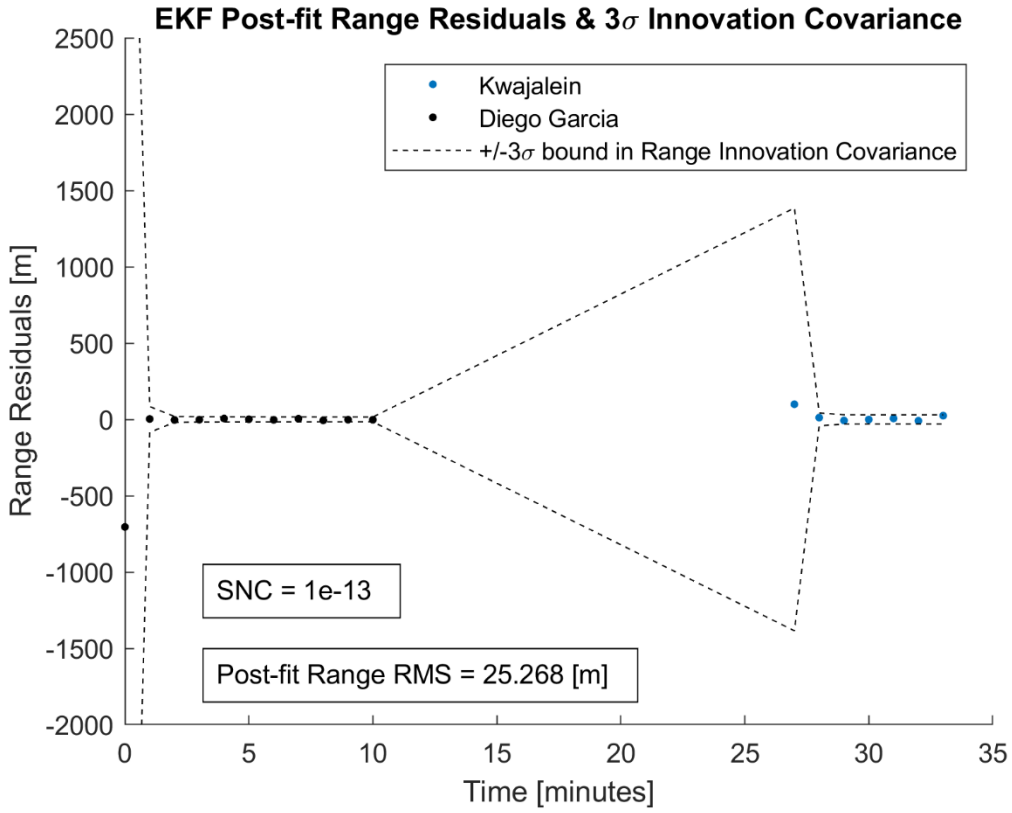


Figure 23: RSO innovations and residuals covariance indicating state convergence after only one measurement.

To reiterate, studying residual behavior to indicate state stability should be used with caution as residuals alone do not guarantee an accurate orbit and thus should be later verified with the traditional state covariance convergence, differences, and arc overlaps.

### DELTA-V CALCULATION

Once the RSO state is resolved post maneuver, back propagation to the maneuver end epoch and simple vector differencing with the nominal trajectory without the maneuver will reveal the $\Delta v$ magnitude and direction. Implementing this method and comparing to states provided by Optus yielded a $\Delta v$ estimate within 0.51 percent of the

reference value. It should be noted that all values are stated in terms of percent error due to the proprietary nature of the estimated parameters. Maneuver type is estimated by comparing orbital elements pre- and post-maneuver as well as decomposing the $\Delta v$ vector into radial, in-track, and cross-track components, resulting in an operator confirmed determination of a North-South station keeping maneuver.

A half-second error is injected into the maneuver start and end epochs to study the solution sensitivity. The results in Table 7 demonstrate the estimation accuracy is reasonably sensitive to the event epochs, placing importance on hypertemporal photometric data collection and the ability to discern when an unmodeled dynamic event has occurred. Many of the techniques discussed in the maneuver detection literature review in Chapter 4 produce $\Delta v$ estimates to within a few tenths of a centimeter per second of the reference value at best.

| Parameter | Accuracy |
|---|---|
| $\Delta v$ magnitude (exact epochs) | Within 0.52 percent of true value |
| $\Delta v$ ( + 0.5 sec. epoch ) | Within 7.85 percent of true value |
| $\Delta v$ ( - 0.5 sec. epoch ) | Within 59.8 percent of true value |
| $\Delta v$ direction | Within 1.72 deg. of true pointing vector |
| Maneuver type | Correct id. of N-S station keeping |
| Maneuver duration | No obs. data to support calculation yet |

Table 7: Delta-v estimation results in terms of percent error of reference values.

The assumption that both the initial and final event epochs are directly observable with photoacoustic sensing is a challenge of its own, but it may become especially problematic for non-impulsive maneuvers associated with long duration, low thrust burns. If one were to only observe an event start or end epoch, it may still be possible to

estimate $\Delta v$ parameters more accurately than the traditional orbit determination methods would have without any precise epoch information. Having one constraint on the trajectory should improve the overall estimation accuracy, but more studies should be conducted to confirm how this extra information can be synthesized with other maneuver estimation techniques.

# Chapter 6

## Spacecraft Operational Assessment

Near real time $\Delta v$ and maneuver type estimation defined in Chapter 5 allow for rapid response to uncooperative satellite operation and anomalous unmodeled dynamic events. Knowledge of the above parameters combined with the known event epochs allow for a deeper understanding of spacecraft operational parameters specific to propulsive events. Through the application of orbital momentum and energy principles about the known maneuver impulse, it will be shown that the prior techniques can be extended to estimate thruster mass flow rate, specific impulse, fuel consumed, and other derived parameters. Knowledge of these parameters will further increase understanding of the active satellite population and support characterization, operational assessment, and ultimately contribute to a safer space environment.

The literature that exists on spacecraft operational parameter estimation is quite limited. Some related research has been completed for mass estimation as in [37] and [38] as well as an effort to determine the mass-specific inertia matrix [39]. The mass estimation methods rely on astrometric and photometric data fusion to disentangle the mass term using refined bidirectional reflectance distribution functions and albedo area-solar radiation pressure models. The mass-dependent results in coming sections demonstrate the importance of continued efforts in the SDA community to estimate RSO mass and the resulting operational assessment capabilities that can be gained from it. As for mass flow rate, fuel consumption, exhaust velocity, and thruster specific impulse, the literature review did not turn up any prior work related specifically to estimating these parameters. However, Klinkrad defines relations for area to mass ratio and size

distribution of solid rocket motor slag that could be potentially be useful if precise engine shut down mass ejection modeling is required [40].

### INTEGRALS OF MOTION

While the origins of the specific orbital momentum and energy integrals of motion are well established [41], it is important to understand their derivation as it has direct implications into the ability to estimate certain spacecraft mass properties. Thus, both principles will be derived and applied to the given parameter estimation problem. Starting with the basis of all orbital motion, Newton's law of gravitation, in Eq. (28) and then finding its relative two-body form via Eq. (29), and assuming the mass of the satellite is negligible to the Earth in this case results in Eq. (30). In general, it is best to make no simplifications when deriving precise quantities dealing with mass terms as is done with the neglection of the satellite mass in Eq. (30). However, in this case it does not matter due to the cancellation that occurs in the following steps.

$$\bar{F}_g = -\frac{GM_E m_{sat}}{r^2}\left(\frac{\bar{r}}{r}\right) \tag{28}$$

$$\ddot{\bar{r}} = -\frac{G(M_E + m_{sat})}{r^2}\left(\frac{\bar{r}}{r}\right) \tag{29}$$

$$\ddot{\bar{r}} = -\frac{\mu \bar{r}}{r^3} \tag{30}$$

Performing the cross product of Eq. (30) with the position vector $\bar{r}$, collecting terms to form Eq. (31), and noticing $\bar{r}$ crossed with itself is zero results in Eq. (32). Equation (32) can be expressed in terms of a differential as in Eq. (33) such that it can be

simplified to the final conservation of specific orbital momentum in Eq. (34) by noticing the derivative is equal to zero.

$$\bar{r} \times \ddot{\bar{r}} + \bar{r} \times \frac{\mu \bar{r}}{r^3} = 0 \tag{31}$$

$$\bar{r} \times \ddot{\bar{r}} = 0 \tag{32}$$

$$\bar{r} \times \ddot{\bar{r}} = \frac{d}{dt}(\bar{r} \times \dot{\bar{r}}) = \bar{r} \times \ddot{\bar{r}} + \dot{\bar{r}} \times \dot{\bar{r}} = 0 \tag{33}$$

$$\bar{r} \times \bar{v} = \bar{h} = constant \tag{34}$$

Similarly, the relative form of the basic two-body equation is manipulated by dotting it with the velocity vector as in Eq. (35) to find the specific orbital energy integral of motion. Noting a useful identity $\bar{r} \cdot \bar{v} = r\dot{r}$ allows for simplification to scalar quantities in Eq. (36).

$$\bar{v} \cdot \dot{\bar{v}} + \bar{v} \cdot \frac{\mu \bar{r}}{r^3} = 0 \tag{35}$$

$$v\dot{v} + \dot{r}\frac{\mu}{r^2} = 0 \tag{36}$$

Recognizing each term in Eq. (36) as a differential yields Eq. (37). Integration of Eq. (37) produces the familiar specific orbital energy integral of motion in Eq. (38).

$$\frac{d}{dt}\left(\frac{v^2}{2} - \frac{\mu}{r}\right) = 0 \tag{37}$$

$$\frac{v^2}{2} - \frac{\mu}{r} = \varepsilon = constant \tag{38}$$

The point of re-deriving these basic quantities is to show that both the momentum and energy equations originate from manipulating the relative two-body equation with either a cross or dot operation with position and velocity. A consequence of this manipulation is that the equations are not linearly independent. This linear dependence will be problematic when attempting spacecraft mass estimation in the next section.

### THRUST PARAMETER ESTIMATION

To infer operational information about an active satellite, the maneuver specific parameters must be related to known orbital quantities. A maneuver is simply an impulse and the initial and final orbital momentum and energy are known quantities from the work of Chapter 5. Thus, it seems plausible to expand the specific orbital momentum and energy equations to their mechanical forms and include the varying work and impulse terms imparted by any unmodeled dynamic events. The most basic forms of the conservation equations are defined in Eq. (39) and Eq. (40).

$$\int_{t_i}^{t_f} F\, dt = mv_f - mv_i = \Delta p \tag{39}$$

$$W = \int_C F \cdot dx = \int_{x(t_i)}^{x(t_f)} F \cdot v\, dt = E_f - E_i \tag{40}$$

Extending these basic equations to the orbit problem and converting to vector quantities while including any rotational terms will yield the expanded forms in Eq. (41) and Eq. (42). These forms assume the only force contributing to the respective work and impulse terms is due to the maneuver and that the satellite mass is now time varying.

$$m_i \bar{r}_i \times \bar{v}_i + \int_{t_i}^{t_f} \bar{r}(t) \times (m_i - \dot{m}t)\bar{a}(t)_{th} dt \; + \int_{t_i}^{t_f} \bar{\tau}(t)\, dt + I_i \bar{\omega}_i + h_i = (m_i - \dot{m}\Delta t)\, \bar{r}_f \times \bar{v}_f + \; I_f \bar{\omega}_f \; + \; h_f \tag{41}$$

$$m_i \left[\frac{1}{2}\bar{v}_i^2 - U_E(\bar{r}_i)\right] + \frac{1}{2}\bar{\omega}_i^T [I_i]\bar{\omega}_i + \int_{t_i}^{t_f} [(m_i - \dot{m}t)\bar{a}(t)_{th}] \cdot \bar{v}(t) dt \; + \int_{t_i}^{t_f} \bar{L}(t) \cdot \bar{\omega}(t) dt = \; (m_i - \dot{m}\Delta t) \left[\frac{1}{2}\bar{v}_f^2 - U_E\left(\bar{r}_f\right)\right] + \; \frac{1}{2}\bar{\omega}_f^T \left[I_f\right]\bar{\omega}_f \tag{42}$$

Effective momentum or energy losses due to imperfect thrust vectoring, momentum wheel saturation, or the change in moment of inertia due to decreasing spacecraft mass are assumed to be negligible for a nadir-pointing, three-axis spin stabilized satellite. Thus, the rotational energy, work, torque, and momentum terms cancel over the time span of the maneuver and can be removed from the equations. The remaining form consists of two equations and five unknowns – mass, mass flow rate, and the position, velocity, and acceleration due to thrust as functions of time during the impulse. To solve for the time varying functions, one can divide the $\Delta v$ magnitude by the burn duration to get the average acceleration magnitude over the maneuver. The direction of the acceleration is the same as the $\Delta v$ pointing vector. Thus, the force model can be augmented to include the acceleration due to the thrust and the satellite position and

velocity as functions of time can be discretized. A fourth order polynomial is then used to fit each component of the discretized state over the maneuver, thus reducing the unknowns from five to two.

With only mass and mass flow rate as the remaining two unknown parameters and two equations, it seems as if it would be possible to solve the system of equations. However, while deriving the specific orbital momentum and energy in the prior section, it is noted that these equations are not linearly independent of each other. This is a key realization because if one attempts to solve for the two unknown parameters, the resulting output will show no unique solution. For this reason, application of momentum and energy to the orbital impulse problem does not allow for standalone estimation of mass and mass-flow rate, thus an *a priori* estimate of one or the other is necessary to solve either equation. What remains are two unknowns and effectively one linearly independent equation. Thus, the assumption is made that a sufficiently accurate *a priori* estimate of mass is known such that the derivation can be completed.

An analytical form of the acceleration due to thrust as a function of time can be formulated based on the specific impulse and rocket equations defined in Eq. (43) and Eq. (44).

$$F_{thrust} = I_{sp} g_0 \dot{m} = m a_{th} \tag{43}$$

$$\frac{\Delta m}{m_i} = 1 - e^{-\Delta v / I_{sp} g_0} \tag{44}$$

Solving for the scalar acceleration due to thrust, vectorizing, and injecting time dependency yields the form in Eq. (45). The acceleration unit vector as a function of time

can either using the polynomial form or the constant $\Delta v$ pointing vector derived in Chapter 5.

$$\bar{a}_{th}(t) = \frac{-\Delta v\, \dot{m}}{(m_i - \dot{m}t)\, ln\left[1 - \frac{\dot{m}\Delta t}{m_i}\right]}\, \hat{a}(t)_{th} \tag{45}$$

Substitution into the simplified mechanical momentum and energy equations yields their final forms in Eq. (46) – (48) below.

$$m_i \varepsilon_i + \int_{t_i}^{t_f} \left[ \frac{-\Delta v\, \dot{m}}{ln\left[1 - \frac{\dot{m}\Delta t}{m_i}\right]}\, \hat{a}(t)_{thrust} \right] \cdot \bar{v}(t) dt = (m_i - \dot{m}\Delta t)\varepsilon_f \tag{46}$$

$$where\ \varepsilon_k = \begin{cases} \frac{1}{2}\bar{v}_i^2 - U_E(\bar{r}_i) & for\ k = i \\ \frac{1}{2}\bar{v}_f^2 - U_E(\bar{r}_f) & for\ k = f \end{cases} \tag{47}$$

$$m_i \bar{r}_i \times \bar{v}_i + \int_{t_i}^{t_f} \bar{r}(t) \times \left[ \frac{-\Delta v\, \dot{m}}{ln\left[1 - \frac{\dot{m}\Delta t}{m_i}\right]}\, \hat{a}(t)_{th} \right] dt = (m_i - \dot{m}\Delta t)\, \bar{r}_f \times \bar{v}_f \tag{48}$$

Utilizing the given Optus spacecraft mass to solve for the mass flow rate included in Eq. (46) yields an estimate within two percent of the true value. Use of Eq. (44) then allows for calculation of the thruster specific impulse and exhaust velocity. It is likely that quantities such as fuel tank feed pressure to thruster inlet are calculable as many formulations of feed pressure equations only depend on mass flow rate. This could be

especially useful if a tank sensor fails and another method is required to monitor pressure. Estimation results are accumulated in Table 8.

| Parameter | Accuracy |
|---|---|
| Mass flow rate | Within 2.0 percent of reference value |
| Specific impulse | Within 3.0 percent of reference value |
| Fuel consumed | Within 1.0 percent of reference value |
| Exhaust velocity | Agrees with thruster class values |

Table 8: Estimation results for the Optus spacecraft operational parameters, in terms of percent error to maintain proprietary nature of propulsion system values.

One method investigated to potentially subvert the linear dependence problem and estimate spacecraft mass utilizes an approach analogous to a Monte Carlo simulation. It is thought that a unique pair of mass and mass flow rate values can maintain conservation of energy and momentum constraints while ensuring the spacecraft state matches the true state at the maneuver end epoch. Thus, a grid of mass and mass flow rate pairs were input to check final system balance in an attempt to isolate which pair of values are the true spacecraft parameters. The conservation of energy equation is chosen for this analysis and thus calculated after each value pair is simulated. In theory, the value that produces a net zero system change in energy would be the unique pair. Results of the minimum energy change search are displayed in Fig. 24. Unfortunately, the solution is ambiguous as there are many mass and mass flow rate pairs that can guide the satellite along the known maneuver trajectory. The minimum energy solutions suggest a linear trend, of which any pair on the local minima line would maintain a net zero energy balance.

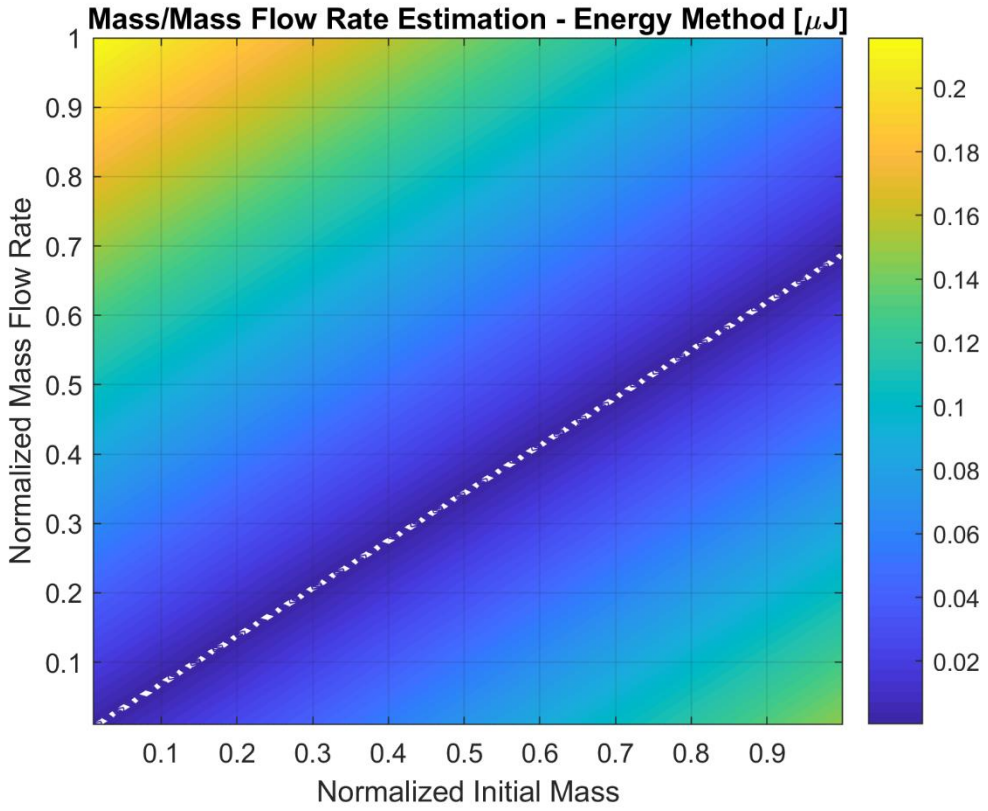


Figure 24: Mass and mass flow rate pair study showing ambiguous local minima.

A less than two percent error for the mass-flow rate estimate is a respectable result for a first-time application of this technique. However, there were many assumptions that went into producing the results that would likely increase the estimation error when applied to experimentally collected data. The worst of the assumptions is likely that the initial and final maneuver event epochs are known to microsecond precision. In an experimental data collection scenario, it may be challenging to discern exactly when these events occur. It does seem likely that a tenth second level event detection would be plausible with kilohertz level sample rates, thus keeping any error within the single digit regime per the Table 7 sensitivity study. In the ExoAnalytics data

referenced in Chapter 2, it is easy to determine the initial event epoch to less than two tenths of a second utilizing only an eight hertz collection rate.

Other likely sources of error include the spacecraft shape model, fidelity of the dynamics, thrust profile averaging, thruster precision, Mt. Stromlo ECEF coordinates, reported burn duration variation, numerical precision in polynomial fits as only fourth order is used, measurement uncertainty, and any remaining unknowns. No propulsion system is a perfect step function as there exist ramp up and down periods in any thrust profile. The acceleration due to thrust is to be assumed a nominal operating average in these simulations and thus loses some realism.

One potential impact of estimating fuel consumption over time is the ability to monitor if an uncooperative satellite is saving enough fuel for a proper post-mission disposal or graveyard orbit. An estimate of specific impulse helps characterize the operational capability of an active satellite. Of course, this research assumes the maneuvers happen at night and the start and end epochs of the propulsive event are directly observable via a ground based optical telescope. It is also assumed that the target RSO can be acquired and tracked within the telescope FOV throughout the event duration. For satellites in LEO this can be a challenge, especially for longer, non-impulsive maneuvers. It seems plausible to employ these tactics to satellites in GEO based on a more stationary orbit. A satellite-to-satellite observation would likely make this method much more feasible as the relative distances and effects of the atmospheric would be lessened, thus increasing the signal-to-noise ratio and thruster event observability.

Assuming the Table 8 parameters are known in addition to the operational frequency derived from spectral analysis and potentially a derived thrust profile, it is

conceivable to compare these propulsion system values to known model specifications and thus constrain a specific class or even unique model to an observed event. Identifying a thruster model may help with other RSO identification parameters such as launch date or country of origin. These results reiterate the importance of efforts in the SSA community to estimate RSO mass and the resulting operational assessments that can be gained through estimates of the Table 8 parameters.

### HYBRID NUMERIC-ANALYTICAL METHODS

The thrust impulse and work integrals contained in Eq. (46) and Eq. (48) were straight forward to solve with MATLAB either analytically or numerically. However, if the impulse term gains complexity or contains additional unknowns, a direct analytical solution may become challenging or computationally intensive. Additionally, estimation of the mass flow rate term requires the parameter to remain analytical which negates the possibility of pure numerical integration. A case where a high order spherical harmonics gravity formulation or rotational torques with a time varying mass moment of inertia is considered in the impulse term could prove problematic to compute.

To subvert this roadblock, one may utilize a hybrid numeric-analytical method. This method can employ the basics of any numerical integration technique while keeping unknown parameters analytical throughout integration. In short, one can numerically integrate "analytically" to overcome computational or complexity challenges. This method is inspired by similar solution efforts that require Taylor or Bessel series expansions and analytical Newton-Rapson iterative approaches in the celestial mechanics community. An example of this hybrid method applied to a simple integral of a function defined as Eq. (49) is shown in Eq. (50). For demonstration purposes and simplicity, the

trapezoidal rule is used to calculate the area under the curve where q is the unknown test parameter to be estimated.

$$f(t) = 2t + q\cos(2t) \tag{49}$$

$$\begin{aligned}\int_{t_i}^{t_f} f(t)dt = {} & \frac{([2t_1 + q\cos(2t_1)] - [2t_i + q\cos(2t_i)])(t_1 - t_i)}{2} \\ & + \frac{([2t_2 + q\cos(2t_2)] - [2t_1 + q\cos(2t_1)])(t_2 - t_1)}{2} \\ & + \cdots + \\ & \frac{([2t_f + q\cos(2t_f)] - [2t_{f-1} + q\cos(2t_{f-1})])(t_f - t_{f-1})}{2}\end{aligned} \tag{50}$$

In keeping the $q$ term analytical, it allows for evaluation of any system of equations the integral is contained in and ultimately the ability to estimate the desired parameter, $q$ in this case but mass flow rate as in Eq. (46) or Eq. (48). The explicit accumulation of terms at each time step will result in a final equation of the form in Eq. (51) where $B$ and $C$ are numerical constants. The basic result is also ideal from a bookkeeping perspective although this will depend on how the unknown parameter to be estimated is defined with respect to the orbital dynamics. After generating the solution form in Eq. (51), a simple root-solve or algebraic solution to the system of equation(s) containing the unknown parameter can be found.

$$\int_{t_i}^{t_f} f(t)dt = B + qC \tag{51}$$

# Chapter 7

# Experimental Data

One of the initial goals of this research is to experimentally observe an active satellite thruster fire event in geosynchronous orbit. If the initial and final maneuver event epochs can be resolved experimentally, it would stand as a proof of concept and further validate the theories postulated herein. Satellite operators at Optus were kind enough to provide their maneuver schedule such that a precise orbital location and epoch were known for each observation attempt. As for the optical systems, the team at the Space Environment Research Center and EOS Space Systems provided the necessary data collection equipment and expertise. At the time of writing, no satellite maneuvers have been experimentally detected and confirmed by the operator yet. However, some anomalous events that are potentially non-propulsive in nature are still under investigation. A summary of the experimental setup and detected phenomena are listed in the following sections. While some of the phenomena listed do not require hypertemporal photometric data or acoustic conversion to be observed or predicted, the data are still included as calibration steps and additional proofs of concept.

## OPTICAL DATA COLLECTION

The optical telescope used is courtesy of the SERC 0.7-meter geotracker at the Mt. Stromlo Observatory in Australia. The hypertemporal sampling rate detector is based on a Hamamatsu PMT sensor (H11901-20) that is sensitive over the entire visible spectrum [42]. The photometric data are sampled at a rate of 50 kHz (capable of rates up to 100 kHz), time stamped in UTC via GPS signal and stored in binary files. The detector is built on the Beaglebone Black PC board with the real time operation software written

in C++. The detector provided data points of averaged intensity values from ten neighboring points and saved the parameter with 12-bit precision at a 20 $\mu s$ interval. Initial sensor calibration steps included closed-dome collection, FOV adjustments, and stellar background considerations.


Figure 25: *(Left)* SLR and space debris tracking facilities at the Mt. Stromlo observatory[9] and *(right)* hypertemporal sampling rate detector developed by D. Kucharski.

**DETECTED EVENTS**

Over twenty hours of data on 29 unique active satellites including the Optus, GLONASS, and Iridium constellations as well as Ajisai, Cosmos 2527, and Sentinel 1a and 1b were collected by the SERC team from 2018-05-29 to 2018-08-16. The team rigorously quantified and removed any noise sources detected by the sensitive equipment. It should be noted that any LEO and MEO observations did not include collaboration with any satellite operators to confirm whether an arc would have a maneuver within the

[9] Imagery obtained from the Mt. Stromlo Observatory Facebook page.

collection period prior to observing. However, if there were an unexplained anomaly in the data, satellite operators at Iridium were kind enough to confirm any correlation to planned maneuvers, if any such correlation existed. Secondary measurement input from LeoLabs also helped supplement whether unexplained signals could be correlated to any RSO unmodeled dynamic events.

Data collected on Iridium 14 revealed a classic flare, or abrupt peak in visual magnitude, due to favorable observation geometry and the relative attitude progression throughout its orbit as indicated in Fig. 26. The flare included two auxiliary peaks on either side of the main peak. It is likely the auxiliary peaks are caused by the door-sized main mission antennas offset by forty degrees from the panel antenna that is known to cause the maximum flare in light intensity[10].

The photoacoustic playback of the flare allows for detection of the main intensity rise and fall as well as the auxiliary peaks. As this is a common satellite event that is easily detected in the photometric domain, the audio playback does not reveal any unique insights besides it being a demonstration of the acoustic domain conversion and an interesting listen. The general aural perception can be described as increasing, then decreasing white noise, with two abrupt transients on the downslope and upslope. One could imagine if a propulsive event occurred during or near a flare that the potential thruster-induced modulation of the flat panel antennas and corresponding harmonics would be easily detectable due to the large apparent visual magnitude over this timespan.

[10] Gupta, O.P., *Iridium – A Global Communication Network*. Retrieved via https://web.stanford.edu/class /aa247/Iridium_Innovations.pdf.

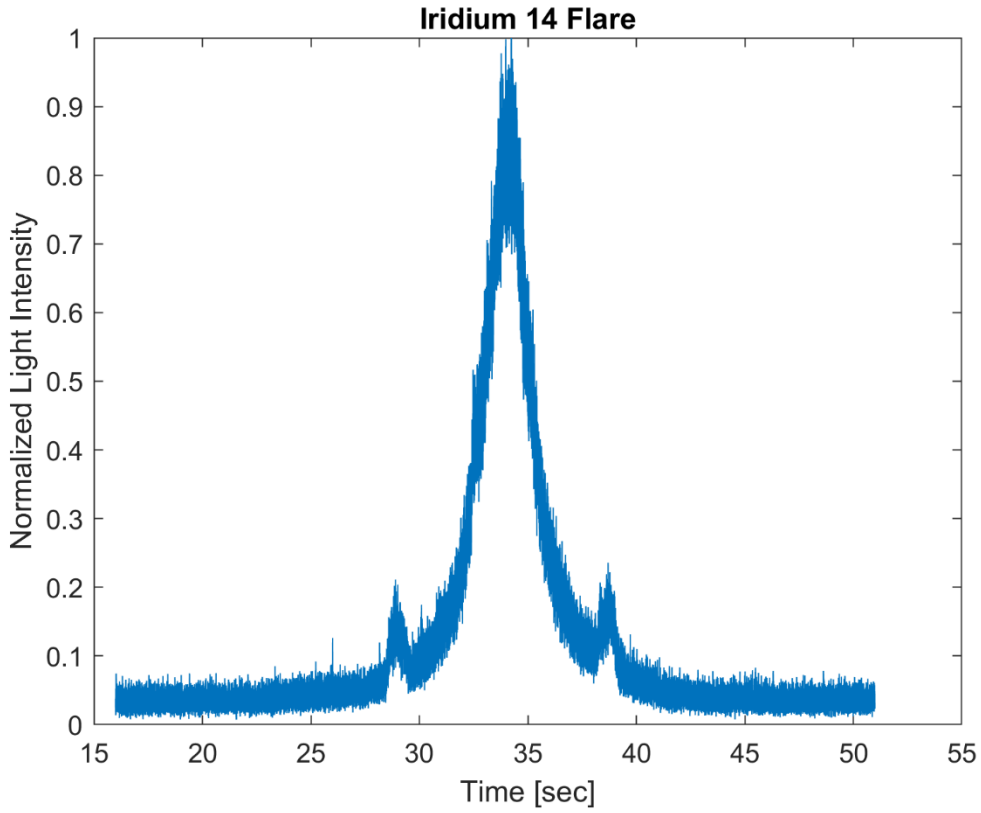


Figure 26: Plot of normalized light intensity for Iridium 14 flare demonstrating two auxiliary peaks, potentially due to the offset door panel antennas.

The Experimental Geodetic Payload satellite also known as Ajisai is a useful calibration object for the photodiode system. Ajisai has a known spin rate of 1.25 Hz and it is one of the dominant signals that can be observed in the Fig. 27. The photoacoustic playback of Ajisai's signal can be described as a "partially muted tumble chirp" that peaks at the indicated rate of 1.25 Hz which is three times the base frequency described in Fig. 27. Like the Iridium flare, this is a relatively well-known phenomenon that is studied in the photometric domain. Also like the Voyager 1 example, the Ajisai tumble chirp audio playback originates from generating an acoustic signal from an event that is

inherently non-acoustic to support analysis and event detection. The acoustic domain conclusions for this observation would simply be a confirmation of typical behavior.

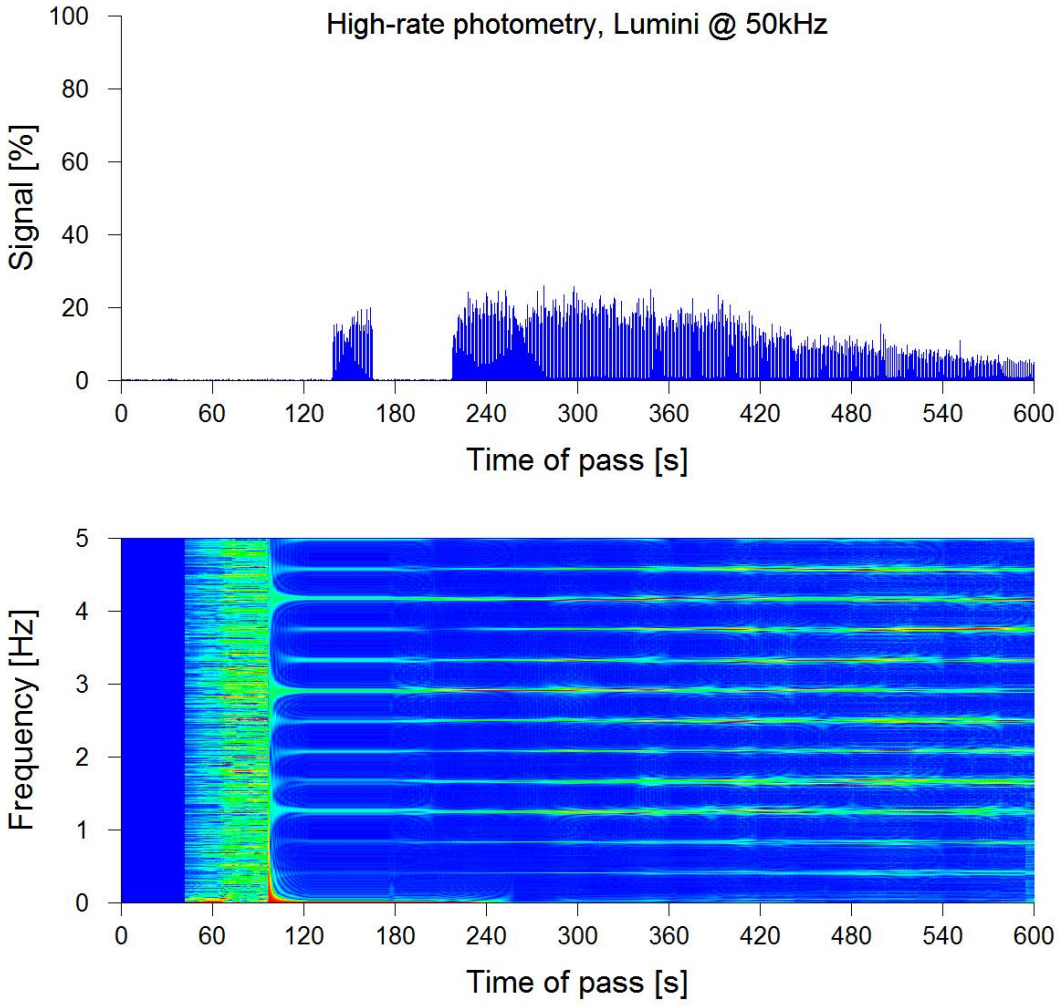


Figure 27: (*Top*) Ajisai pass light intensity peaks over time. (*Bottom*) Frequency spectrum obtained with the open source FFTW tool[11] courtesy of D. Kucharski. The parallel lines indicate the harmonics of the satellite spin frequency signal of 0.4167 Hz.

[11] Frigo, M. and Johnson, S. G., *FFTW subroutine*. Accessed via http://www.fftw.org/.

Collecting photoacoustic data on a decommissioned satellite that has a spin rate like Ajisai could yield unique signatures. One could imagine the spin induced “crackling” sound the multi-layer thermal insulation blankets (MLI) could produce on the decommissioned satellite would be unique compared to the clean tumble chirp generated by the non-flexible mirrors mounted on the exterior surface of Ajisai. It should also be noted that the FFTW algorithm used in Fig. 27 does well in removing the low frequency power components, resolving the concern from Chapter 4 when discussing the realism of the simulated 58 Hz signal.

In many of the collected data arcs, a 10 Hz and sometimes a 60 Hz signal would show up briefly and then disappear with no apparent correlation to satellite events. The signal itself sounds like a “reverberating tick” that is easily identifiable whenever it appeared. Eventually, it was discovered that the nearby satellite laser ranging equipment operation correlated exactly with the signal epochs. While the SLR operated at 60 Hz, the photometric system became blind during the laser pulses approximately every 100 ms due to what is likely a time domain aliasing effect. Thus, the 10 Hz signal can be acquired in the FFT. An example of the 60 Hz detection is shown via spectrogram in Fig. 28.

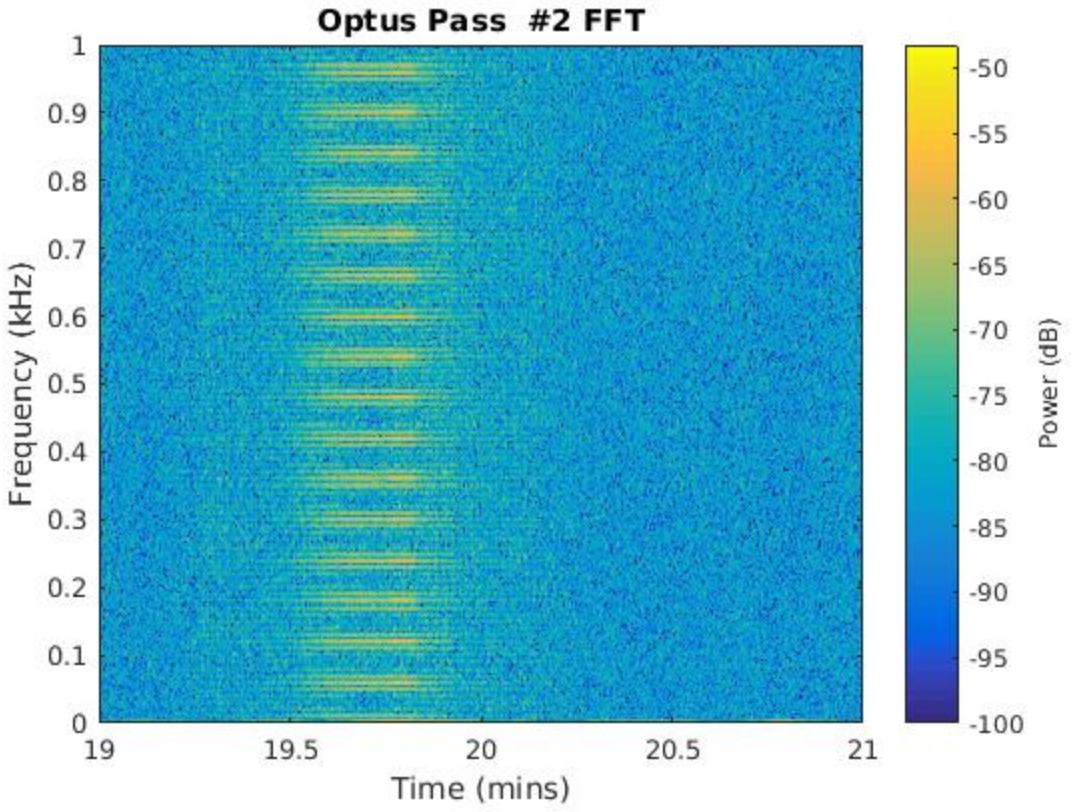


Figure 28: Spectrogram demonstrating the 60 Hz laser pulse fundamental frequency and harmonics detected when the SLR field of view crossed the geotracker FOV.

The most exciting false positive signal detected is caused by a tracking stability problem as the telescope operated at maximum speed while the tracked satellite was at a high elevation angle above the local horizon. It looked as if there were some sort of pre-ignition sequence event detected due to a minor peak approximately 6.5 seconds before the main light intensity increase. The signal in Fig. 29 looks quite like the abrupt peak that would be expected for a thruster plume detection, as well as the exponential “thrust profile-like” tail off.

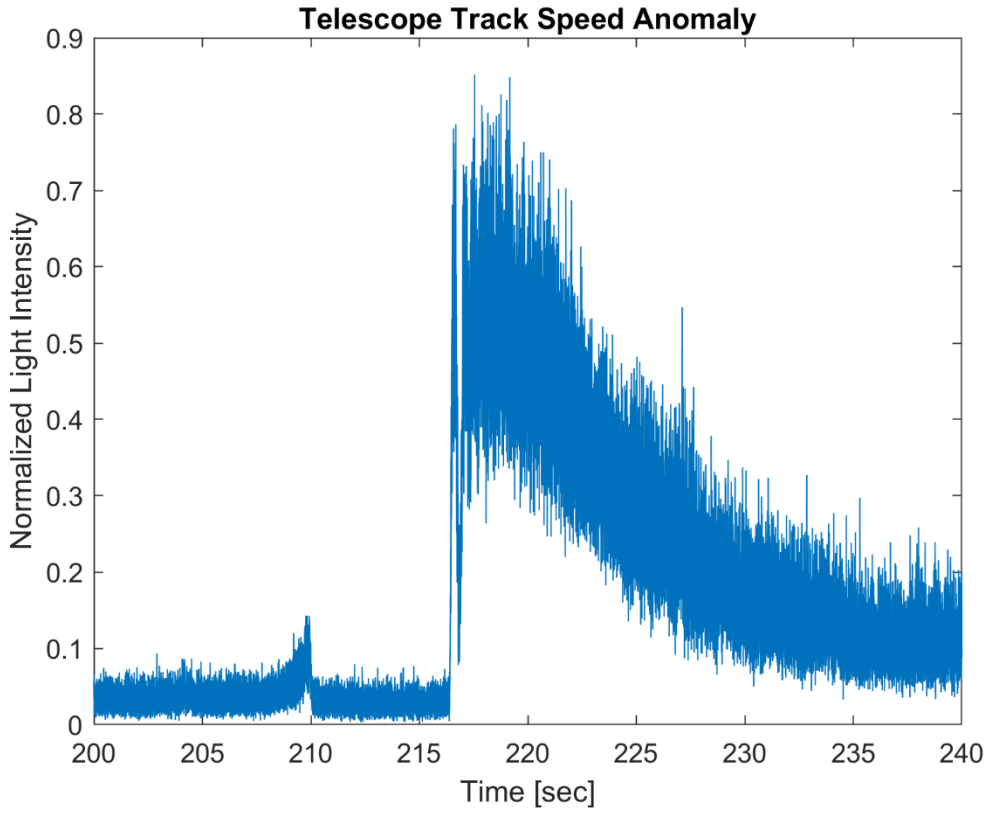


Figure 29: Light intensity plot showing the abrupt peak caused by the telescope track stability problem described above.

Another mystery signal is explained by the Australian power grid that operates at 50 Hz. A commonly observed phenomenon is the flickering of exterior lights in close proximity to the observatory at two times the grid frequency as shown in Fig. 30. The lights are motion sensor activated and thus can show up sporadically in the data. It is likely that some curious kangaroos in the vicinity activated the motion sensor that controls the exterior lights. While this error source did contribute to signal randomness, it was not a common occurrence and did not change the assumption that atmospheric effects were still the dominant source of uncertainty.

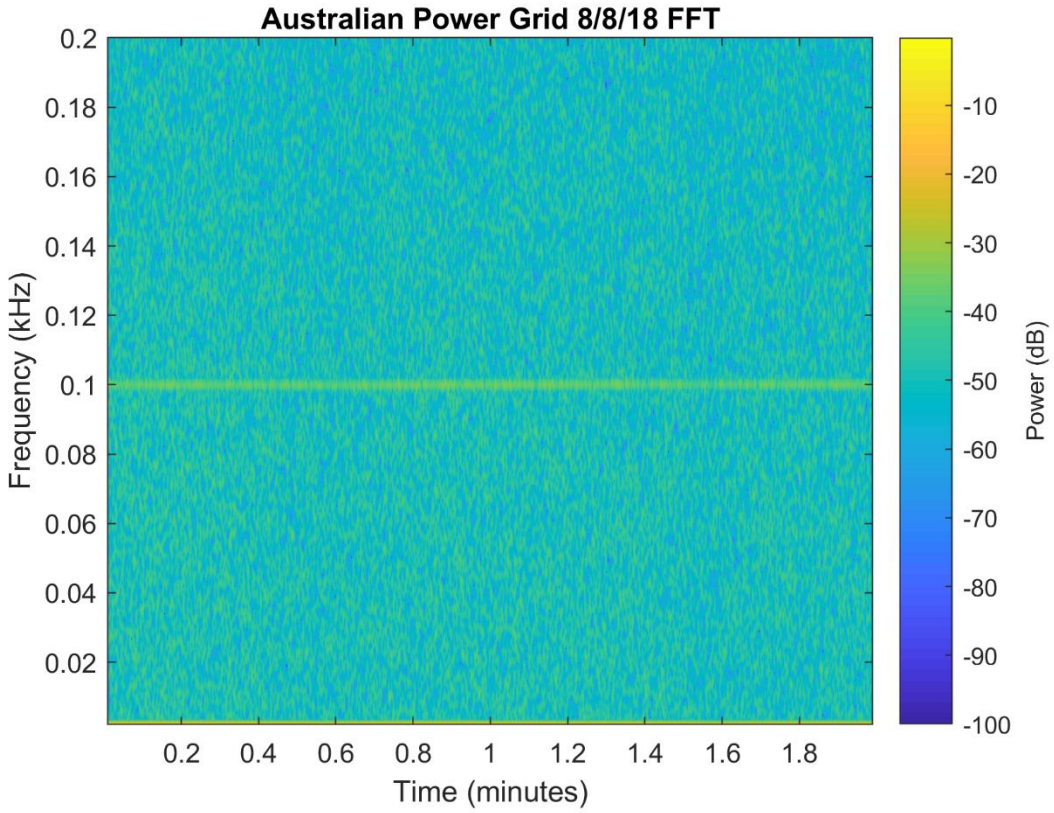


Figure 30: FFT that detected the Australian power grid lights flickering at 2x the 50 Hz power grid frequency.

A unique signal that remains unexplained occurred five times in two different satellite constellations. Iridium 14 had four instances and Sentinel 1b had another similar instance and each event could be described as a short "burst" transient. Each time the profile appeared in the data there were two distinguishable peaks as seen in Fig. 31. There were many other cases where a star passed the FOV which caused a gradual rise and fall in light intensity. The transients seem much too quick to be explained by a star passing. Acoustic playback of the potential events sounds somewhat noisy but does have a detectable "dual burst" or "knock" characteristic to it. It is possible these are some sort of measurement system aberration.

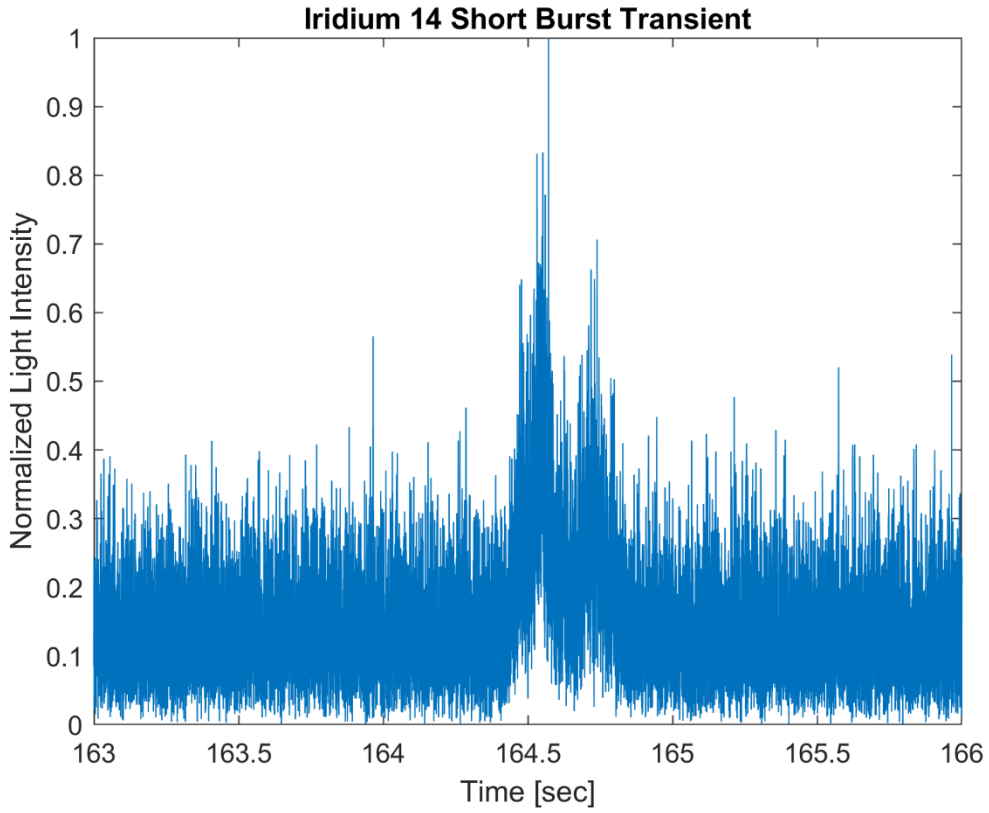


Figure 31: Unexplained Iridium 14 dual peak “burst” event detection.

The frequency content is quite rich in the sub-20 Hz range as displayed in Fig 32. It has been confirmed by the satellite operators that the photoacoustic signature was not caused by a maneuver. However, it was left undefined as to if the potential event correlated to any other on-board component operation. To justify the resources spent reviewing satellite event logs for a potential correlation, further collection on additional inactive satellites to determine if this signal profile appears is required. If the signal did reoccur, a non-propulsive component activation can be ruled out as the source.

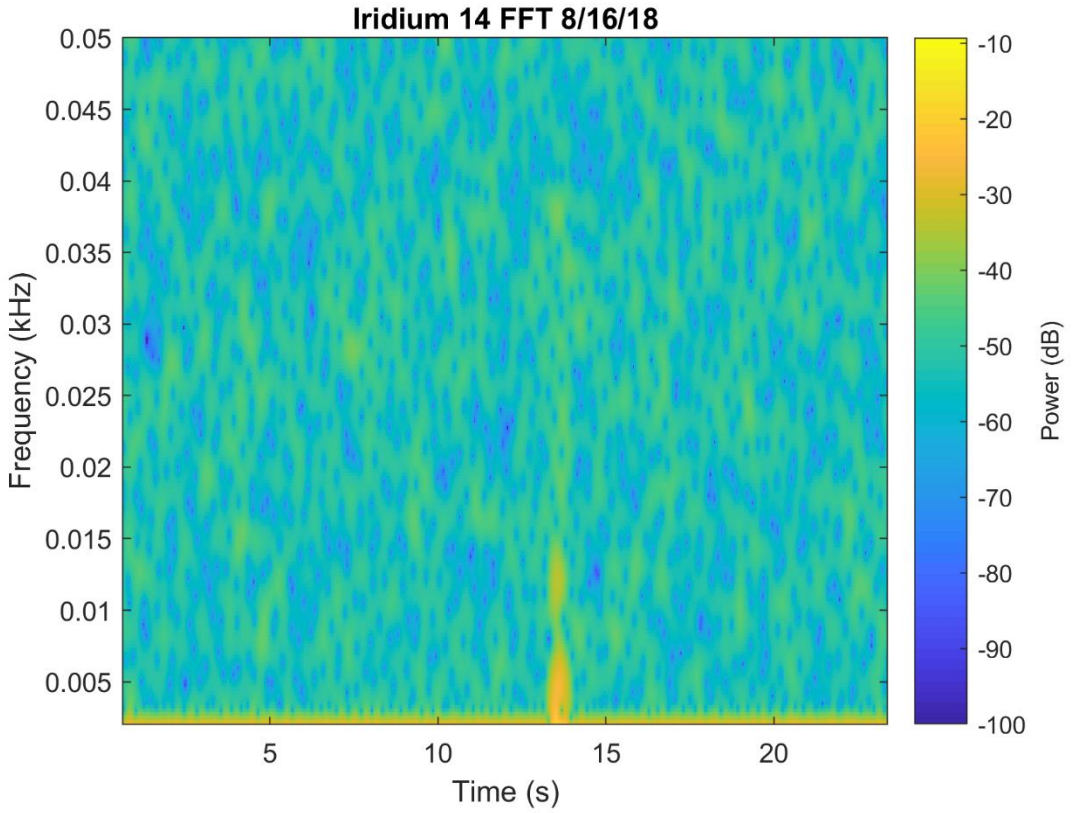


Figure 32: Uncorrelated Iridium 14 short "burst" transient displaying rich frequency content below 20 Hz.

# Chapter 8

# Conclusions

This thesis serves to demonstrate the benefits that can be gained by exploiting remote photoacoustic signatures to support satellite characterization and operational assessment. Photoacoustic signatures were defined as the acoustic playback of hypertemporal photometric data and the conversion from light to sound was detailed in Chapter 2. Luminance data from high frame rate rocketry footage was processed as acoustic data as a proof of concept and achieved realistic results. In Chapter 3, photoacoustic sensing case studies were evaluated as a method to uniquely identify on-board active satellite events at a subsystem level and to support characterization of RSOs.

A synthetic light curve simulation of an active satellite undergoing a maneuver was generated and analyzed in Chapter 4. A range of box-wing satellite body displacement magnitudes were simulated to study the minimum event displacement detection criteria. It was demonstrated that by modeling the effects of the atmospheric noise as a best-case $\mathcal{N}(0,0.03^2)$ distribution on the apparent visual magnitude, sub-1.0 cm displacement values were detectable through implementation of a custom cross-correlation search algorithm. The signal-to-noise ratio for this best-case scenario was approximately -27.55 dB, as it also was for the $\mathcal{N}(0,0.04^2)$ apparent visual magnitude case which may suggest a lower bound on the SNR value.

Chapter 5 applied an Extended Kalman Filter to demonstrate an approximately converged spacecraft state within at most five minutes of maneuver termination epoch. Photoacoustic sensing provided direct event epoch time stamps that were previously unavailable with prior techniques. These epochs were assumed accurate to within a few tenths of a second and utilized to accurately calculate the $\Delta v$ magnitude and direction to

within 0.52 percent and 1.72 percent of the true values provided by the Optus satellite operators respectively. The maneuver was also correctly identified as a N-S station keeping maneuver.

The principles of conservation of orbital energy and momentum were then applied in Chapter 6 to further the operational assessment study. It was shown that the momentum and energy equations are not linearly independent in the mechanical form and thus an *a priori* mass estimate is required. It was then demonstrated that with the given assumptions, the mass flow rate for a maneuver can be estimated to within two percent of the reference value. Specific impulse and fuel consumed were also derived to within three and one percent of their reference values respectively. With these newly estimated parameters, it becomes plausible to consider active spacecraft fuel monitoring for proper post-mission disposal orbit adherence. The thrust parameters may allow for constraints to be placed on unique propulsion system component models or be used for spacecraft diagnostics and health assessment. Chapter 7 presented the results of experimental data collection attempts and calibration efforts with certain anomalous events remaining uncorrelated.

In summary, the methodologies researched as part of this thesis have been proven technically robust via simulation and analysis. Some of the ideas presented have initiated new lines of inquiry yet to be investigated. Applied experimental opportunities remain open for exploration and a confirmed on-orbit maneuver detection awaits proof of concept. Ultimately, the research presented herein provides a foundation for further understanding of the space environment. If applied operationally, the demonstrated techniques support efforts to maintain a more efficient and sustainable space domain for long-term human spaceflight operations.

## FUTURE WORK

The simulations presented in Chapter 4 suggest that it is quite plausible that on-board satellite events can be detected with hypertemporal photometric data. Data collection efforts from industry colleagues support these claims as do the Iridium 14 and Sentinel 1b anomalies discussed in Chapter 7. Further investigation into telemetry logs at anomaly epochs remain the logical next steps for satellite operators to confirm any subsystem event correlation.

The limiting factor in space event detection capability is the effect of the turbulent atmosphere on the apparent visual magnitude and light intensity values. If a more advanced adaptive optics scheme were applied along with a narrower FOV to improve the SNR, it is likely that the minimum detectable satellite body vibration displacement threshold $d_{body}$ can be further improved. This may allow for more frequent experimental detections and ideally prove credible at GEO distances. A satellite-to-satellite observation application would reap the benefits of little to no atmosphere, likely only limited by the optical equipment precision.

A detection of active satellite maneuvers in LEO and GEO confirmed by an operator should remain the experimental goal to continue demonstrating photoacoustic sensing as a near real time event detection methodology. It would also be interesting to further research standalone mass estimation, data fusion, or some other technique that eliminates the need for an *a priori* mass estimate to produce the Chapter 6 results. Additionally, it seems that hypertemporal photometric data are an appropriate candidate for machine learning, pattern recognition, and biometric analysis in support of unique RSO event identification. Utilizing the acoustic perception of the data would be a beneficial human-machine interface training synthesis.

# Appendix A

# Publications

Some of the content included in this thesis has been submitted to peer-reviewed scientific journals for publication or presented at conferences. A summary of the various sources is included below for reference.

### CONFERENCE PRESENTATIONS

[43] Spurbeck, J., Jah, M., Kucharski, D., Bennet, J., Webb, J. "Satellite Characterization, Classification, and Operational Assessment Via the Exploitation of Remote Photoacoustic Signatures." Advanced Maui Optical and Space Surveillance Technologies Conference, Maui, Hawaii, 2018.

[44] Spurbeck, J., and Jah, M. K., "Near Real Time Satellite Event Detection and Characterization with Remote Photoacoustic Signatures," 2019 Space Traffic Management Conference, 2019.

### SUBMITTED TO REFEREED JOURNALS

Journal of Astronautical Sciences – submitted as full paper with the same title as in [43].

# Glossary

CSpOC – Combined Space Operations Center

ECI – Earth Centered Inertial reference frame

ECEF – Earth Centered Earth Fixed reference frame

EKF – Extended Kalman Filter

FFT – Fast Fourier Transform

FOV – Field of View

GEO – Geosynchronous Earth Orbit, orbital belt at 35,786 km

GLONASS – Global Navigation Satellite System

GMAT – General Mission Analysis Tool

IAU – International Astronomical Union

J2000 – Epoch used to define the ECI frame

JPL – NASA Jet Propulsion Laboratory

LEO – Low Earth Orbit, defined as an orbit with an altitude less than 2,000 km

MEO – Medium Earth Orbit, defined from 2,000 km to 35,786 km

NASA – National Aeronautics and Space Administration

RSO – Resident Space Object

SERC – Space Environment Research Centre

SDA – Space Domain Awareness

SNR – Signal-to-Noise Ratio

SPICE – an observation geometry system for space science missions developed by JPL

SLR – Satellite Laser Ranging

SSA – Space Situational Awareness

UTC – Coordinated Universal Time

# References

[1] Bell, A.G., “On the Production and Reproduction of Sound by Light.” American Journal of Sciences, Third Series, vol. XX, no. 118, Oct. 1880, pp. 305-324.

[2] Slater, D., Ridenoure, R., Klumpar, D., Carrico, J., and Jah, M. “Light to Sound: The Remote Acoustic Sensing Satellite (RASSat).” 30th Annual AIAA/USU Conference on Small Satellites, Logan, Utah, 2016.

[3] International Telecommunications Union. *Parameter values for the HDTV standards for production and international programme exchange.* ITU-R BT.709-6. June 2015. Retrieved from https://www.itu.int/dms_pubrec/itu-r/rec/bt/R-REC-BT.709-6-201506-I!!PDF-E.pdf.

[4] Dennis, J., Yu, Q., Tang, H., Tran, H., and Li, H. “Temporal coding of local spectrogram features for robust sound recognition,” Acoustics, Speech and Signal Processing (ICASSP), 2013 IEEE International Conference, 26-31 May 2013 DOI: 10.1109/ICASSP.2013.6637759.

[5] The Agency for Science, Technology and Research (A*STAR). "Audio processing: Computers following the brain's lead." ScienceDaily. ScienceDaily, 6 November 2013. Retrieved from www.sciencedaily.com/releases/2013/11/131106084430.htm.

[6] Davis, A., et. al., “The Visual Microphone: Passive Recovery of Sound from Video,” ACM Transactions on Graphics, vol. 33, Issue 4, Article No. 79.

[7] Gurnett, D.A., Kurth, W.S., Burlaga, L.F., and Ness, N.F. “In Situ Observations of Interstellar Plasma with Voyager 1,” Science, vol 341, pp. 1489-1492. 12 September 2013, DOI: 10.1126/science.1241681.

[8] NASA Jet Propulsion Laboratory, *Sounds of Mars: NASA's InSight Senses Martian Wind*. Accessed via https://mars.nasa.gov/resources/22201/sounds-of-mars-nasas-insight-senses-martian-wind/?site=insight.

[9] Slater, D., "Passive long range acousto-optic sensor," Proc. of SPIE Vol. 6304.

[10] Xu, M., and Wang, L. V., "Photoacoustic imaging in biomedicine," Rev. Sci. Instrum. 77, 041101 (2006); https://doi.org/10.1063/1.2195024.

[11] Grinvald; et al. (1986). "Functional architecture of cortex revealed by optical imaging of intrinsic siPhoto-acoustic and Video-acoustic Methods for Remote Sensing of Distant Sound Sourcesgnals". Nature. 324 (6095): 361–364. Bibcode:1986Natur.324..361G. doi:10.1038/324361a0. PMID 3785405.

[12] Tserevelakis, George J., et. al, "Photoacoustic imaging reveals hidden underdrawings in paintings," Scientific Reports 737, Vol. 7, Is. 1, 10.1038/s41598-017-00873-7.

[13] Sayigh, Laela. (2013). Cetacean Acoustic Communication. Biocommunication of Animals. 275-297. 10.1007/978-94-007-7414-8_16.

[14] Wyse, L., "Audio Spectrogram Representations for Processing with Convolutional Neural Networks," Proceedings of the First International Conference on Deep Learning and Music, Anchorage, US, May, 2017 (arXiv:1706.08675v1 [cs.NE]).

[15] P. Verma and J. O. Smith, "Neural Style Transfer for Audio Spectrograms," Jan. 2018.

[16] Jain, A., Ross, A., and Prabhakar, S. "An Introduction to Biometric Recognition," IEEE Transactions on Circuits and Systems for Video Technology, vol 14, No. 1, January 2004.

[17] Adeoye, O. “A Survey of Emerging Biometric Technologies,” International Journal of Computer Applications, vol. 9, No. 10, November 2010.

[18] Kelecy, T., and Jah, M., “Detection and orbit determination of a satellite executing low thrust maneuvers.” Acta Astronaut, vol. 66, 2010, pp.798–809.

[19] Aaron, B.S., “Geosynchronous satellite maneuver detection and orbit recovery using ground based optical tracking.” Masters Thesis, Massachusetts Institute of Technology, 2006.

[20] Kelecy, T., Hall, D., and D, S. M., “Satellite Maneuver Detection Using Two-Line Element (TLE) Data,” Advanced Maui Optical and Space Surveillance Technologies Conference, Maui Economic Development Board, Wailea, HI, 2007.

[21] Patera, R. P., “Space Event Detection Method,” Journal of Spacecraft and Rockets, Vol. 45, No. 3, 2008, pp. 554, 559, doi:10.2514/1.30348.

[22] Holzinger, M. J., Scheeres, D. J., and Alfriend, K. T., “Object Correlation, Maneuver Detection, and Characterization Using Control-Distance Metrics,” Journal of Guidance, Control, and Dynamics, Vol. 35, No. 4, 2012, pp. 1312, 1325, doi:10.2514/1.53245.

[23] Hujsak R (2005) Reverse engineering maneuvers. In: AGI 2005 User’s conference, Washington, DC.

[24] Zhang ZJ, Dong YF (2008) Autonomic detection method of space target orbit maneuver based on wavelet analysis. J Beijing Univ Aeronaut Astronautics 34(3):353–356.

[25] K, H., “Maneuver Detection and Estimation with Optical Tracklets,” Advanced Maui Optical and Space Surveillance Technologies Conference, Maui Economic Development Board, Wailea, HI, 2014.

[26] Lee, S., and Hwang, I., "Interacting Multiple Model Estimation for Spacecraft Maneuver Detection and Characterization," AIAA Guidance, Navigation, and Control Conference, AIAA SciTech Forum, Kissimmee, FL, 2015, pp. 103–115.

[27] Wetterer, C.J., and Jah, M. "Attitude Estimation from Light Curves," Journal of Guidance, Control, and Dynamics, vol. 32, No. 5, 2009, pp. 1648-1651.

[28] Mallik, V. Modified Cook-Torrance reflectance model, "*sunpointedflatplate*," MATLAB code.

[28] Haugse. E. D., Juengst, C. D., Salus, W. L., and Lollock, J. A., "On orbit system identification," Structural Dynamics and Materials Conference and Exhibit, 37th, Salt Lake City, UT, Apr. 15-17, 1996, Technical Papers. Pt. 4. (A96-26801 06-39)

[29] Personal communications. Dr. Tamara Payne, Applied Optimization, Inc. July 2018.

[30] Vallado, David A. Fundamentals of Astrodynamics and Applications. Microcosm Press, 2013, Print. Fourth Edition.

[31] International Earth Rotation and Reference Systems Service (IERS). *Technical Bulletins and Technical Notes.* Retrieved from https://www.iers.org.

[32] MATLAB Aerospace Toolbox, "gravityspherical harmonic," modified EGM-96 gravity field code.

[33] Vallado, D., "Sun" and "moon" functions. 27 May 2002.

[34] General Mission Analysis Tool – Users Guide, R2013a. Goddard Space Flight Center. http://gmat.sourceforge.net/doc/R2013a/help-a4.pdf.

[35] Conjunction Data Message Recommended Standard CCSDS 508.0-B-1 BLUE BOOK, June 2013.

[36] Tapley, B. D., Schutz, B. E., Born, G. H., Statistical Orbit Determination. Elsevier Inc., 2004.

[37] Mallik, V., Jah, M.K. Reconciling space object observed and solar pressure albedo-areas via astrometric and photometric data fusion. Adv. Space Res. (2018), https://doi.org/10.1016/j.asr.2018.08.005.

[38] R. Linares, M. Jah, J. Crassidis, F. Leve, T. Kelecy, "Astrometric and photometric data fusion for inactive space object mass and area estimation," J. Int. Acad. Astronaut.: Acta Astronaut., 99 (2014), pp. 1-15.

[39] Linares, R., Leve, F. A., Jah, M. K., and Crassidies, J. L., "Space object mass-specific inertia matrix estimation from photometric data," Proceedings of the 35th Annual AAS Rocky Mountain Section Guidance and Control Conference, Vol. 144, p. 41-54.

[40] Klinkrad, H., *Space Debris, Models and Risk Analysis*, first edition. Praxis Publishing.

[41] Curtis, H. D., *Orbital Mechanics for Engineering Students*, Second Edition. Elsevier Aerospace Engineering Series, 2010.

[42] Kucharski, D., High sampling-rate photometric detector, Space Environment Research Centre (SERC). Developed in 2018.

[43] Spurbeck, J., Jah, M., Kucharski, D., Bennet, J., Webb, J. "Satellite Characterization, Classification, and Operational Assessment Via the Exploitation of Remote Photoacoustic Signatures." Advanced Maui Optical and Space Surveillance Technologies Conference, Maui, Hawaii, 2018.

[44] Spurbeck, J., and Jah, M. K., "Near Real Time Satellite Event Detection and Characterization with Remote Photoacoustic Signatures," 2019 Space Traffic Management Conference, 2019.

# Vita

Justin Spurbeck was born and raised in Alaska before eventually moving to Minnesota, where he stayed until completion of his undergraduate degree. Justin graduated with a Bachelor of Aerospace Engineering and Mechanics and a minor in astrophysics from the University of Minnesota in 2014. He gained invaluable experience working as a Graduate Research Assistant for the NASA Jet Propulsion Laboratory supporting flight dynamics software validation for Exploration Mission 1 (EM-1) while pursuing a master's degree at the University of Texas at Austin. He also became a seasoned Satellite Navigation Systems Intern working in industry for DigitalGlobe focusing on orbit determination, conjunction assessment, and dual-frequency carrier phase GPS data analysis.

Email address: jspurbeck@utexas.edu

This thesis was typed by Justin A. Spurbeck.